

The Interferometric Binary Cnc in Praesepe: Precise Masses and Age

Leslie M. Morales, Eric L. Sandquist, Gail H. Schaefer, Christopher D. Farrington, Robert Klement, Luigi R. Bedin, Mattia Libralato, Luca Malavolta, Domenico Nardiello, Jerome A. Orosz, et al.

▶ **To cite this version:**

Leslie M. Morales, Eric L. Sandquist, Gail H. Schaefer, Christopher D. Farrington, Robert Klement, et al.. The Interferometric Binary Cnc in Praesepe: Precise Masses and Age. The Astronomical Journal, 2022, 164, 10.3847/1538-3881/ac7329 . insu-03780756

HAL Id: insu-03780756
https://insu.hal.science/insu-03780756

Submitted on 20 Sep 2022

HAL is a multi-disciplinary open access archive for the deposit and dissemination of scientific research documents, whether they are published or not. The documents may come from teaching and research institutions in France or abroad, or from public or private research centers.

L'archive ouverte pluridisciplinaire **HAL**, est destinée au dépôt et à la diffusion de documents scientifiques de niveau recherche, publiés ou non, émanant des établissements d'enseignement et de recherche français ou étrangers, des laboratoires publics ou privés.

The Astronomical Journal, 164:34 (22pp), 2022 August https://doi.org/10.3847/1538-3881/ac7329
© 2022. The Author(s). Published by the American Astronomical Society.
OPEN ACCESS

The Interferometric Binary ϵ Cnc in Praesepe: Precise Masses and Age

Leslie M. Morales[1], Eric L. Sandquist[1], Gail H. Schaefer[2], Christopher D. Farrington[2], Robert Klement[2], Luigi R. Bedin[3], Mattia Libralato[4], Luca Malavolta[3,5], Domenico Nardiello[3,6], Jerome A. Orosz[1], John D. Monnier[7], Stefan Kraus[8], Jean-Baptiste Le Bouquin[7,9], Narsireddy Anugu[2], Theo ten Brummelaar[2], Claire L. Davies[8], Jacob Ennis[7], Tyler Gardner[7], and Cyprien Lanthermann[2]

[1] San Diego State University, Department of Astronomy, San Diego, CA 92182, USA; lmorales9028@sdsu.edu
[2] The CHARA Array of Georgia State University, Mount Wilson Observatory, Mount Wilson, CA 91023, USA
[3] Istituto Nazionale Astrofisica di Padova—Osservatorio Astronomico di Padova, Vicolo dell'Osservatorio 5, I-35122 Padova, Italy
[4] AURA for the European Space Agency (ESA), ESA Office, Space Telescope Science Institute, 3700 San Martin Drive, Baltimore, MD 21218, USA
[5] Dipartimento di Fisica e Astronomia "Galileo Galilei," Universitá di Padova, Vicolo dell'Osservatorio 3, Padova I-35122, Italy
[6] Aix Marseille Univ, CNRS, CNES, LAM, Marseille, France
[7] Astronomy Department, University of Michigan, Ann Arbor, MI 48109, USA
[8] Astrophysics Group, Department of Physics & Astronomy, University of Exeter, Stocker Road, Exeter, EX4 4QL, UK
[9] Institut de Planetologie et d'Astrophysique de Grenoble, Grenoble F-38058, France
Received 2022 April 6; revised 2022 May 18; accepted 2022 May 19; published 2022 July 5

Abstract

We observe the brightest member of the Praesepe cluster, ϵ Cnc, to precisely measure the characteristics of the stars in this binary system, en route to a new measurement of the cluster's age. We present spectroscopic radial velocity measurements and interferometric observations of the sky-projected orbit to derive the masses, which we find to be $M_1/M_\odot = 2.420 \pm 0.008$ and $M_2/M_\odot = 2.226 \pm 0.004$. We place limits on the color–magnitude positions of the stars by using spectroscopic and interferometric luminosity ratios while trying to reproduce the spectral energy distribution of ϵ Cnc. We reexamine the cluster membership of stars at the bright end of the color–magnitude diagram using Gaia data and literature radial velocity information. The binary star data are consistent with an age of 637 ± 19 Myr, as determined from MIST model isochrones. The masses and luminosities of the stars appear to select models with the most commonly used amount of convective core overshooting.

Unified Astronomy Thesaurus concepts: Open star clusters (1160); Spectroscopic binary stars (1557); White dwarf stars (1799); Stellar evolution (1599); Long baseline interferometry (932)

Supporting material: machine-readable table

1. Introduction

Absolute age measurements for stars are fraught with difficulties because comparisons with theoretical models are required, and because our knowledge of important factors like the initial chemical composition, or the stellar masses, or even the behavior of certain basic physical processes is often poor. Often, even when we are able to precisely measure characteristics of stars that can speak to a star's age, these gaps in our understanding result in substantial systematic errors. Star clusters provide an environment where difficulties like chemical composition uncertainties can be mitigated and a uniform age is usually a good assumption. The study of binary systems within such clusters can give the opportunity to evaluate stellar masses in a precise way.

The goals of this paper are to precisely characterize stars (including masses) at the turnoff of the open cluster Praesepe and derive a precise age for the cluster from these stars in order to set up Praesepe as an age-calibration standard. There are a number of astrophysically interesting features of the cluster that recommend it for attention. The rotation of the main-sequence stars has been studied extensively, among the A-type stars (McGee et al. 1967; Abt & Willmarth 1999; Debernardi et al. 2000; Fossati et al. 2007, 2008; Cummings et al. 2017), solar-type stars (Delorme et al. 2011; Kovács et al. 2014), and low-mass stars (Scholz & Eislöffel 2007; Agüeros et al. 2011; Scholz et al. 2011; Douglas et al. 2017). These measurements establish Praesepe as a gyrochronology age standard, although a more precise absolute age would improve its utility. Among the A stars, there are a number of interesting phenomena like δ Scuti pulsation (e.g., Belmonte et al. 1994; Hernandez et al. 1998; Frandsen et al. 2001; Breger et al. 2012) and surface chemical peculiarities (Abt 1986; Burkhart & Coupry 1998; Hui-Bon-Hoa & Alecian 1998; Fossati et al. 2007, 2008). The cluster has a fairly large population of white dwarfs (WDs), with 12 known (Salaris & Bedin 2019). Almost all of the WDs have spectroscopically measured masses, and they cover a fairly large range from about 0.7 to 0.9 $M_\odot$ (Cummings et al. 2018; Salaris & Bedin 2019), in contrast to the field WD population. These WDs probably originate from progenitor stars in a fairly narrow mass range, where the stars ignite core helium burning in a nondegenerate gas but do not undergo a second dredge-up convection event that helps limit the size of the core.

To these ends, we have conducted a thorough analysis of the known double-lined spectroscopic binary star system ϵ Cnc (also known as Meleph, HD 73731, 41 Cnc, BD +20 2171). With the combined light of its stars, ϵ Cnc is one of the brightest members of Praesepe. Plaskett et al. (1921) were the first to measure the velocity of the second component of the binary, but Abt & Willmarth (1999) were the first to fit the spectroscopic orbit of the system, finding a period of 35.202 days. Both stars in the binary are rotating relatively modestly

Original content from this work may be used under the terms of the Creative Commons Attribution 4.0 licence. Any further distribution of this work must maintain attribution to the author(s) and the title of the work, journal citation and DOI.

for A-type stars, and both stars appear to show surface chemical peculiarities (Burkhart & Coupry 1998). But most importantly, the binary is bright enough, is close enough, and has a wide enough orbit that the orbit can now be resolved with interferometric methods and a precise measurement of the masses of the component stars is within reach. Further, the system's color implies that both stars are on or near the very brightest part of the main sequence, with the brighter star likely to be near the end of its core hydrogen burning life. Because the brighter star is starting to evolve more rapidly than its companion, its characteristics are sensitive functions of age.

In Section 2, we discuss the spectroscopic, photometric, and interferometric data used, as well as the measurement of the radial velocities of the stars. In Section 3, we describe the fitting method used to determine the characteristics of the stars, like the masses. In Section 4, we discuss the age measurement for Praesepe and its applications to other areas of stellar astrophysics, like the WD initial−final mass relation (IFMR).

1.1. Reddening, Distance, and Metallicity

Taylor (2006) critically examined measurements of Praesepe's reddening and settled on $E(B-V) = 0.027 \pm 0.004$. This is consistent with the reddening derived by Gaia Collaboration et al. (2018) from isochrone fitting. Zero reddening is sometimes used for the cluster (e.g., Cummings et al. 2017, 2018), but we believe that this is ruled out by comparisons with the Hyades. The chemical compositions and ages of these two clusters are extremely similar, but without a significant reddening for Praesepe, the main sequences do not align, and there are troubling offsets between the WD initial −final mass sequences (Salaris & Bedin 2019). Douglas et al. (2019) used a spectroscopic examination of FGK stars in Praesepe and Hyades and found a reddening value $E(B-V) = 0.011 \pm 0.004$ between zero and the Taylor value.

The weighted average parallax for Praesepe members in Gaia DR2 was determined as 5.371 ± 0.003 mas (Gaia Collaboration et al. 2018) or 5.361 ± 0.005 mas (Cantat-Gaudin et al. 2018). There are a number of studies indicating that Gaia parallaxes are systematically offset to smaller values (and implying that objects are systematically closer than Gaia indicates; Lindegren et al. 2018; Zinn et al. 2019), however. In this paper, we employ the Gaia Early Data Release 3 (EDR3), which may have a smaller parallax offset of -17 μas than DR2 (Lindegren et al. 2021). Based on a simple selection of members within 5° of the cluster center, 6 mas yr^{-1} of the cluster's proper-motion vector, and parallax within 0.4 mas of an iteratively determined average, we find $\bar{\omega} = 5.424$ mas. This implies a distance modulus $(m-M)_0 = 6.33 \pm 0.02$.

Recent spectroscopic examinations of Praesepe stars agree well that the cluster is quite metal-rich, similar to the Hyades. Most of the narrow-lined A-type stars in the cluster show chemical peculiarities (e.g., Burkhart & Coupry 1998) and so are not appropriate for indications of the mean cluster abundances. However, giants and solar-type stars should have deep enough surface convection zones that chemical diffusion effects would be mostly erased. Yang et al. (2015) find $[Fe/H] = +0.16 \pm 0.06$ from four giant stars, while Carrera & Pancino (2011) find $[Fe/H] = +0.16 \pm 0.05$ from three giants. Boesgaard et al. (2013) find $[Fe/H] = +0.12 \pm 0.04$ from 11 solar-type stars, while D'Orazi et al. (2020) find $[Fe/H] = +0.21 \pm 0.01$ from 10 solar-type dwarfs. Finally, Cummings et al. (2017) find $[Fe/H] = +0.156 \pm 0.066$ from 39 F, G, and K dwarfs, and Vejar et al. (2021) find $[Fe/H] = +0.21 \pm 0.02$ from six stars with spectral types between G5 and F8.

1.2. Review of Literature Ages

In the most recent studies of Praesepe, the age of the cluster has been calculated to range from 590 to 800 Myr. This is due to debates over the cluster's metallicity and the effects of stellar rotation. Gáspár et al. (2009) tested different metallicities in isochrone modeling using PADOVA isochrones and derived an age of 757 ± 36 Myr using $[Fe/H] = +0.2$.

Praesepe and Hyades are often studied together because it is widely understood that these are nearly coeval clusters and because of their similarity in characteristics such as metallicity. Brandt & Huang (2015) asserted the importance of understanding stellar rotation in discussing these clusters because it can cause chemical mixing in their brightest main-sequence stars. They argue that if stellar rotation is neglected, it creates inconsistencies in age in the Bayesian color–magnitude technique that was used to date the clusters using PARSEC models. The age of the cluster becomes more consistent in the models when rotation is taken into account. They derived an older age of 800 Myr using $[Fe/H] = +0.12$.

On the other hand, Gossage et al. (2018) used MESA models to examine rotating and nonrotating color–magnitude diagrams (CMDs) of Praesepe. In contrast to Brandt & Huang (2015), they conclude that the best-fit isochrone is not one with rotation but rather a younger nonrotating one, estimating an age of 590 Myr using $[Fe/H] = +0.24$.

The relative age difference between Praesepe and the Hyades can also be estimated using gyrochronology of solar-type stars. Hyades stars rotate more slowly on average than Praesepe stars do, leading to a determination that Praesepe is about 57 Myr younger than the Hyades (Douglas et al. 2019).

2. Observations and Analysis

2.1. Spectroscopy

The majority of the radial velocity measurements in this study are based on a reanalysis of spectra taken as part of a survey of bright Praesepe stars by Abt & Willmarth (1999). The spectra were obtained on the Kitt Peak National Observatory (KPNO) 0.9 m coudé feed telescope and spectrograph between 1991 and 1996. The spectra generally covered the wavelength range 436–474.2 nm, at a resolution of about 0.022 nm. Abt & Willmarth obtained a double-lined spectroscopic orbit of ϵ Cnc at the time, although they noted that the rotationally broadened lines of the two stars are always blended. To improve the accuracy of the radial velocities, we performed a new analysis of the spectra, as detailed in Section 3.

In addition, we extracted two spectra from the archive of the ELODIE spectrograph at the Observatoire de Haute-Provence (OHP). The spectra (R = 42,000) were taken in 2004 by observer R. Monier, covering the range 385–681 nm.

Finally, we obtained four new spectra in 2020 with the Fiber-fed Echelle Spectrograph (FIES) on the 2.56 m Nordic Optical Telescope (NOT). Two spectra each were obtained near predicted radial velocity extremes in order to better resolve the stars individually and improve the measurement of the velocity amplitude for later determination of the masses. We used the medium-resolution (R = 46,000) fiber in our

observations, covering the spectral range 370–830 nm (Telting et al. 2014), although we only used 440–660 nm in our measurements. We processed the images and extracted one-dimensional spectra using FIESTool (ver. 1.5.1). The wavelength calibration was done using exposures of the ThAr lamp taken immediately before the science exposures. Individual spectral orders were continuum normalized before being merged.

2.1.1. Literature and Newly Measured Radial Velocities

Literature radial velocities are available for the primary star in ϵ Cnc from several sources, but many of these were rejected owing to likely effects of blending of the lines of the two stars. Plaskett et al. (1921) report measurements at four epochs in 1919 and 1920 from the 1.83 m Plaskett Telescope at Dominion Astrophysical Observatory (DAO), including one claiming detection of both stars. The detection of double lines occurred approximately at one velocity extremum ($\phi \approx 0.14$), and the velocity separation of the measurements agrees well with our modern solution if a -6.5 km s^{-1} offset is used. We therefore regard the detection as legitimate and utilize the measurement with the offset applied. The remaining measurements were discarded as affected by blending.

Abt (1970) reported eight measurements taken at Mt. Wilson Observatory in 1923, although we only used five of these. The remaining three measurements with phases $0.1 < \phi < 0.3$ show clear signs of blending. Finally, there were 10 epochs observed by Abt & Willmarth (1999) for which the original spectra have not been recovered. In those cases, the reported velocities were still used in the fitting of a velocity solution. These literature values are reported along with our measurements in Tables 7 and 8. Julian dates reported by Plaskett et al. (1921) and UT dates reported by Abt (1970) were converted to heliocentric Julian dates.

Radial velocity measurements were made using broadening functions (BFs; Rucinski 1992) derived from the spectra. We used the program BF-rvplotter (Rawls 2016) to calculate the BFs for each spectrum after modifying the code to fit rotational BFs (rather than Gaussians) to the two star profiles. The BFs are calculated through a comparison with a nonrotating synthetic spectrum of similar temperature and surface gravity, which in this case came from Coelho et al. (2007). Because of the particular combination of radial velocity separations and rotational broadening for the two stars, we found that the broadening profiles of the stars overlapped substantially and produced significant correlations between the measured rotation and radial velocities. As a result, we found it necessary to determine rotational velocities for the two stars from spectra with the highest signal-to-noise ratios and velocity separations. We subsequently fixed the values of the rotational velocities and refitted all spectra to derive the radial velocities we present. Heliocentric velocity corrections were applied to all calculated velocity values.

2.1.2. Rotational Velocity and Luminosity Ratio

Figure 1 shows the BFs calculated from the spectra with the cleanest separation of the two stars' peaks. These 11 spectra were taken close to velocity extremes and gave very consistent measurements for the widths of the rotational BF fits (Table 1). We derived weighted averages of the primary and secondary star's velocity widths from these spectra: $v_A \sin i = 48.0 \pm 0.2$ km s^{-1} and $v_B \sin i = 76.5 \pm 0.2$ km s^{-1}. The stars are probably rotating considerably slower than single stars of similar brightness in the cluster (see Table 5). If the stars have aligned rotation axes, then the system cannot be close to synchronism because the primary has a lower measured rotational velocity.

As we will find in Section 2.3, the stars of ϵ Cnc have similar surface temperatures, and in that situation, the BF areas for the two stars give an indication of the relative luminosities. We therefore used our fits of the spectra in Table 1 to estimate the luminosity ratio of the two stars in the visible wavelength range, complementing measurements in the infrared from interferometry below. We restricted the rotational velocity fitting to a $\pm 1\sigma$ range around the weighted averages determined above and redid the fits for the BF heights in order to derive the areas. The results are given in Table 1, where the average ratio (with the error in the mean) is 0.622 ± 0.010. This is in agreement with the infrared ratios (see Table 3), supporting the idea of very similar surface temperatures.

2.2. Interferometry

Although lunar occultations of ϵ Cnc have been observed several times (Peterson & White 1984; Peterson et al. 1989), the system was not previously resolved. As we will see from the modeling below, this is largely due to a confluence of aggravating factors: a high inclination, an orientation of the orbit that strongly foreshortens the major axis, and a mostly north–south alignment of the minor axis (putting it fairly close to perpendicular to the ecliptic). These issues have made interferometric observations necessary to resolve the orbit.

Our interferometric observations were obtained from the Center for High Angular Resolution Astronomy (CHARA) at Mt. Wilson Observatory using two different beam combiners called CLIMB and MIRC-X (ten Brummelaar et al. 2005). The CLIMB beam combiner is a broadband, single spectral channel instrument that optimizes sensitivity and is a three-beam expansion of the CLASSIC two-beam combiner (Ten Brummelaar et al. 2013). The MIRC-X instrument is an image-plane combiner that simultaneously combines the light from up to six telescopes and works well on faint binary companions (Anugu et al. 2020). In the low-resolution ($R = 50$) configuration we used, MIRC-X observes in eight different spectral channels (Kraus et al. 2018). The CLIMB data were reduced using the pipeline developed by J. D. Monnier, with the general method described in Monnier et al. (2011) and extended to three beams (e.g., Kluska et al. 2018). The MIRC-X data were reduced using the standard MIRC-X pipeline version 1.3.5.[10]

The log of the observations is given in Table 2, along with the number of fringe visibility (two-telescope interference) and closure phase (derived from the phase shifts in the fringe patterns for three-telescope groups) measurements. Fringe visibilities as a function of projected baseline provide information about the separation and orientation of the two stars in the binary, as well as their relative brightnesses. Visibilities are calibrated using observations on the same night of unresolved single stars. The calibrators are listed in the table, and the observed visibilities were compared to predicted visibilities (based on model angular diameters for a uniformly illuminated disk; Bourges et al. 2017) to derive the normalization for ϵ Cnc observations. The assumed diameters for the listed calibrators can be found in the JMMC Stellar Diameters Catalog V2. To ensure that the calibrators are unresolved and fringe visibility is at its maximum for atmospheric

[10] https://gitlab.chara.gsu.edu/lebouquj/mircx_pipeline

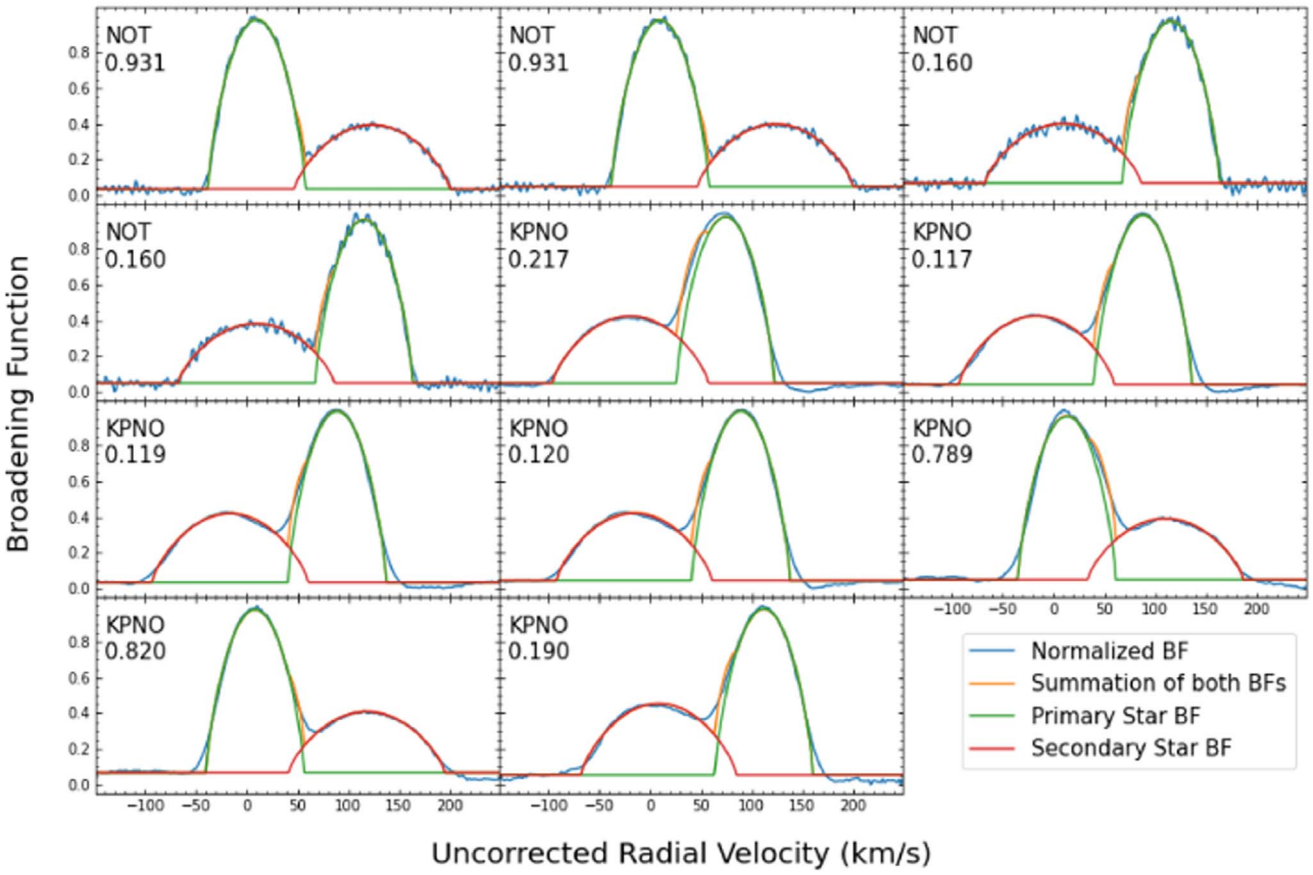


Figure 1. Broadening profiles for the spectra with the most distinguishable contributions from the two stars, with orbital phase given in the upper right corner. The lines show the fits to the primary star profile (green), the secondary star profile (red), the normalized fit (blue), and the summation (orange). The first four panels are from NOT FIES spectra, and the last seven panels are from KPNO spectra.

Table 1
Rotational Velocity and Luminosity Ratio Measurements for ϵ Cnc

mJD[a]	Phase ϕ	$v_A \sin i$ (km s^{-1})	$v_B \sin i$ (km s^{-1})	L_B/L_A	Source
48638.824	0.217	47.23 ± 0.08	76.26 ± 0.22	0.680	KPNO
49021.874	0.117	48.83 ± 0.08	75.31 ± 0.19	0.642	KPNO
49021.931	0.119	48.94 ± 0.08	75.56 ± 0.22	0.639	KPNO
49021.980	0.120	48.43 ± 0.08	75.27 ± 0.25	0.628	KPNO
49080.622	0.789	48.77 ± 0.07	77.56 ± 0.22	0.593	KPNO
49081.706	0.820	48.86 ± 0.08	76.29 ± 0.25	0.595	KPNO
49094.698	0.190	48.29 ± 0.08	76.57 ± 0.23	0.683	KPNO
58960.375	0.931	47.05 ± 0.07	77.41 ± 0.26	0.604	NOT FIES
58960.379	0.931	47.05 ± 0.07	77.49 ± 0.27	0.600	NOT FIES
58968.404	0.160	47.70 ± 0.07	77.02 ± 0.21	0.590	NOT FIES
58968.408	0.160	47.15 ± 0.07	76.96 ± 0.21	0.585	NOT FIES

Note.
[a] mJD = HJD –2,400,000.

conditions, those with diameters less than 0.5 mas were chosen. In almost all cases, calibration observations were taken before and after observations of ϵ Cnc. In the CLIMB observations, visibilities were measured simultaneously in several combined output beams for the same pairs of telescopes, and we treated the resulting visibility measurements as independent. Closure phases are observables that provide information about asymmetry in the light distribution and can provide more powerful measures of the luminosity ratio for the stars in a binary.

Our CLIMB observations were conducted in *K* band, and our MIRC-X observations in *H* band (in eight subchannels), so they give us relative luminosity information for the component stars in the two wavelength regions. Most of our CLIMB observations were affected by marginal weather that made position measurements difficult, but the interferometry still provides observational limits of value to the orbit determination.

2.3. Spectral Energy Distributions

ϵ Cnc does not have eclipses, and so to get additional information on the component stars, we need to utilize photometry. There is an abundance of calibrated photometry

Table 2
Log of Interferometric Observations of ϵ Cnc

UT Date	mJD Start[a]	Combiner	N_{tel}	N_{vis}	N_{clos}	Calibrators
2017 Jan 31	57784.77	CLIMB	3	9	3	HD 73785, 73819
2018 Feb 05	58154.76	CLIMB	3	42	6	HD 72779, 74379
2018 Feb 06	58155.86	CLIMB	3	41	6	HD 72779, 74379
2018 Nov 19	58441.99	CLIMB	3	21	3	HD 72779
2018 Nov 25	58448.02	CLIMB	3	14	2	HD 72779
2018 Dec 13	58465.94	CLIMB	3	28	4	HD 73344, 73533, 74379
2018 Dec 24	58476.85	CLIMB	3	26	4	HD 73344
2019 Nov 08	58795.85	MIRC-X	5	512	448	HD 72779, 73533, 74379
2019 Dec 13	58830.98	MIRC-X	5	272	184	HD 72779
2021 Feb 24	59269.78	MIRC-X	5	320	320	HD 72779, 73533
2021 Mar 25	59298.75	MIRC-X	5	320	320	HD 72779
2021 Mar 29	59302.69	MIRC-X	6	480	640	HD 72779, 74379, 82394
2021 Apr 03	59307.67	MIRC-X	6	480	640	HD 72779, 82394, 74379
Total				2496	2570	

Note.
[a] mJD = HJD –2,400,000 at start of observation sequence.

for the binary that we use below to characterize the spectral energy distribution (SED) of the stars.

Ultraviolet: Ultraviolet is particularly important for characterizing A-type stars at the turnoff of the Praesepe cluster. We obtained photometry from the Galaxy Evolution Explorer (GALEX; Martin et al. 2005) archive in the far-UV (FUV; 1344–1786 Å) passbands. The cluster was imaged in the FUV for 3329 s as part of a guest investigator program (GI1 proposal 48, P.I. M. Burleigh). Morrissey et al. (2007) describe the characteristics of the GALEX photometry and its calibration to flux. GALEX magnitudes are on an AB system (Oke & Gunn 1983), and we used the zero-point magnitudes ($m_{FUV} = 18.82$) and reference fluxes (1.40×10^{-15} erg s^{-1} cm^2 Å^{-1}, respectively) to convert to flux.

The cluster was observed by the Astronomical Netherlands Satellite (ANS) in five ultraviolet bands centered at 1550, 1800, 2200, 2500, and 3300 Å. Magnitudes and measurement errors were taken from Wesselius et al. (1982) and are directly related to monochromatic fluxes. The absolute flux calibration is described in de Boer & Wesselius (1980).

Optical, Near-ultraviolet, and Near-infrared: There are several sources for narrow- and broadband photometry in and near the optical range. We obtained narrowband Strömgren *uvby* photometry for cluster stars from Paunzen (2015), and we employed reference fluxes from Gray (1998) to convert the magnitudes to fluxes. Kazlauskas et al. (2006) presented seven-filter Vilnius photometry of cluster stars, and we converted the reported magnitudes to fluxes using the zero-points from Mann & von Braun (2015). Observations in the Geneva system were taken from the Catalog of Stars Measured in the Geneva Observatory Photometric System (Rufener 1988, 4th edition). Observations in the Johnson 13-color system can be found in Johnson & Mitchell (1975), and reference fluxes for the conversion from magnitudes to fluxes were taken from the Spanish Virtual Observatory (SVO) Filter Profile Service (Rodrigo et al. 2012; Rodrigo & Solano 2020). Additionally, there are spectrophotometric observations of many bright Praesepe stars in 16 very narrow passbands in Clampitt & Burstein (1997). These observations are tabulated as colors relative to measurements in their 5556 Å filter.

Photoelectric photometry in Johnson *UBVRI* filters was taken from Morel & Magnenat (1978) and the AAVSO Photometric All-Sky Survey (APASS; Henden 2019, Data Release 10), which also included Sloan $g'r'i'$ filters. The *UBVRI* measurements were converted to fluxes using reference magnitudes from Table A2 of Bessell et al. (1998), accounting for the known reversal of the zero-point correction rows for f_λ and f_ν. Observations on the four-color *WBVR* system came from Kornilov et al. (1991), with flux calibration again making use of Mann & von Braun (2015) references. Photometry in the Tycho filters B_T and V_T was taken from the Tycho Reference Catalogue (Hog et al. 1998), with absolute flux calibration information taken from Mann & von Braun (2015). Due to the brightness of the binary and other cluster members, there are only *u*, *g*, and *r* measurements in the Sloan Digital Sky Survey (SDSS; York et al. 2000). We used point-spread function magnitudes from Data Release 14, calibrated according to Finkbeiner et al. (2016). The SDSS is nearly on the AB system, with small offsets in u_{SDSS} and z_{SDSS} that we have also corrected for here. The APASS $g'r'i'$ filters are on an AB system similar to the SDSS and were calibrated the same way.

Finally, Gaia has already produced high-precision photometry extending far down the main sequence of the cluster as part of Early Data Release 3. We obtained the fluxes in the *G*, G_{BP}, and G_{RP} bands from the Gaia Archive.

Infrared: We have obtained Two Micron All Sky Survey (2MASS; Skrutskie et al. 2006) photometry in JHK_s from the All-Sky Point Source Catalog and have converted these to fluxes using reference fluxes for zero magnitude from Cohen et al. (2003). We also used photometry in all four bands (W1, W2, W3, W4) from the Wide Field Infrared Explorer (WISE; Wright et al. 2010), which were also converted to fluxes using tabulated reference fluxes at zero magnitude. An additional measurement in the S9W filter at 8.22 μm was taken from AKARI satellite IRC all-sky survey data (Ishihara et al. 2010).

Some clues to the CMD positions of the two stars in the binary come from luminosity ratios derived from the BF fits in the visible part of the spectrum (see Section 2.1.2) and from the interferometry in the infrared *H* and *K* bands. These ratios all return values near 0.6, implying very similar temperatures and clearly restricting the stars to the upper part of the main sequence. If the spectroscopically measured luminosity ratio

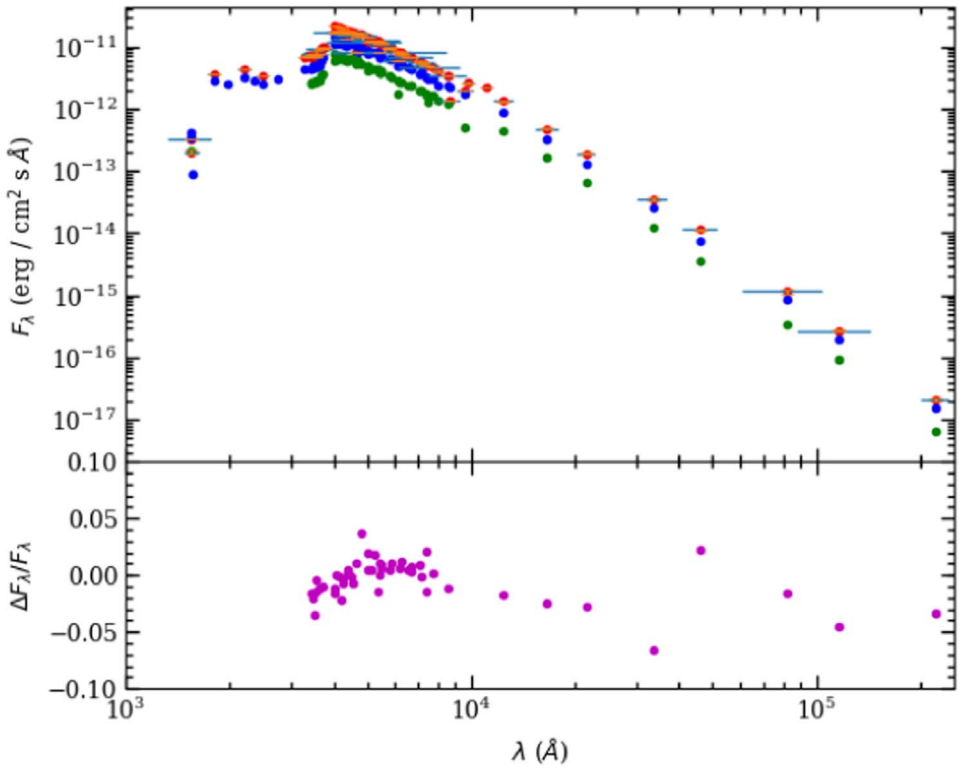


Figure 2. Top: SED for the binary ϵ Cnc from photometry (red points) and for the best-fit main-sequence stars (HD 73819 with blue points and HD 73711 with green points increased in flux by a factor of 1.1). Horizontal error bars represent the effective width of the filter. Bottom: fractional difference between the binary star photometry fluxes and the best-fit sum of main-sequence stars.

applies to the Gaia G magnitude, then the two stars of ϵ Cnc should have $G = 6.784 \pm 0.007$ and $G = 7.324 \pm 0.011$. The primary should therefore be among the stars at the bright end of the CMD gap ($6.8 < G < 7.4$), and the secondary should be approximately 0.2 mag brighter than the faint end of the gap.

To put further limits on the components of the binary, we can check whether existing cluster members can act as proxies, such that the binary's SED is reproduced when the SEDs of the two stars are added together. To find the best proxy for ϵ Cnc A, we considered the five cluster objects that are closest in magnitude to ϵ Cnc A (HD 73210, HD 73575, HD 73712, HD 73785, HD 73819; see Figure 2). As discussed in Appendix A.1, we first looked for signs of binarity, which would affect the CMD position. The two redder stars (HD 73575 and the possible triple HD 73712) are too red to reproduce the color of ϵ Cnc in combination with a main-sequence companion. One of the remaining stars grouped near $(G_{BP} - G_{RP}) = 0.27$ (HD 73210) is a double-lined spectroscopic binary with a fairly extreme mass ratio ($q \approx 0.35$; Abt & Willmarth 1999). The final two stars (HD 73785 and HD 73819) are the best candidates for a proxy star.

To find the best proxy for ϵ Cnc B, we examined stars at the bright end of the main sequence. We first checked for binarity and considered whether they could be blue stragglers that are beyond the end of the main sequence in this cluster. The three brightest main-sequence stars (HD 72846, HD 72942, and HD 73711) are discussed in Appendix A.1. Two of the stars (HD 72942 and HD 73711) show chemical peculiarities that are often associated with binarity, but only HD 72942 has a clearly detected companion.

We added the SEDs of different bright and faint proxy star candidates together to see whether they could reproduce the SED of the binary, and we found that the combination of HD 73819 and HD 73711 agreed best. Because the spectroscopic luminosity ratio implies that the fainter component of ϵ Cnc B is brighter than any of the cluster turnoff stars, we scaled the SED of HD 73711 upward by 10% to account for this. Figure 2 shows the best match. The bottom panel shows that we are able to reproduce the binary's SED to within about 5% in filter bands stretching from the ultraviolet far into the infrared. Redder stars at the brightness level of ϵ Cnc A produce stronger mismatches as a function of wavelength and can be ruled out. We believe that this provides sufficient localization of the two stars to make some use of CMD positions as part of our analysis of ϵ Cnc.

As shown in Figure 3, the brighter of the proxy stars (EP Cnc or HD 73819) falls among a few stars that appear to be single stars near core hydrogen exhaustion, while the fainter proxy star (HD 73711[11]) appears to be close to the populated bright end of the main sequence. Clustering of stars in the CMD may indicate an evolutionary slowdown. Thus, there is an elevated probability that the primary star of ϵ Cnc would be in such a phase.

To get an indication of the properties of ϵ Cnc A, we fit the photometric SED of HD 73819 with ATLAS9 models (Castelli & Kurucz 2003),[12] as shown in Figure 4. We used models with fixed values [Fe/H] = +0.2 and $\log g = 3.6$, where the surface gravity was chosen from an MIST evolutionary track because there is some sensitivity to gravity in the ultraviolet shortward

[11] Coincidentally, HD 73711 is cited as a distant companion to ϵ Cnc in the Washington Double Star Catalog (Mason et al. 2001). We cannot ascribe any significance to the apparent similarity between HD 73711 and the fainter component of ϵ Cnc though.

[12] Models were calculated using the ATLAS9 Fortran code that employed updated 2015 line lists and used temperatures between the published grid points.

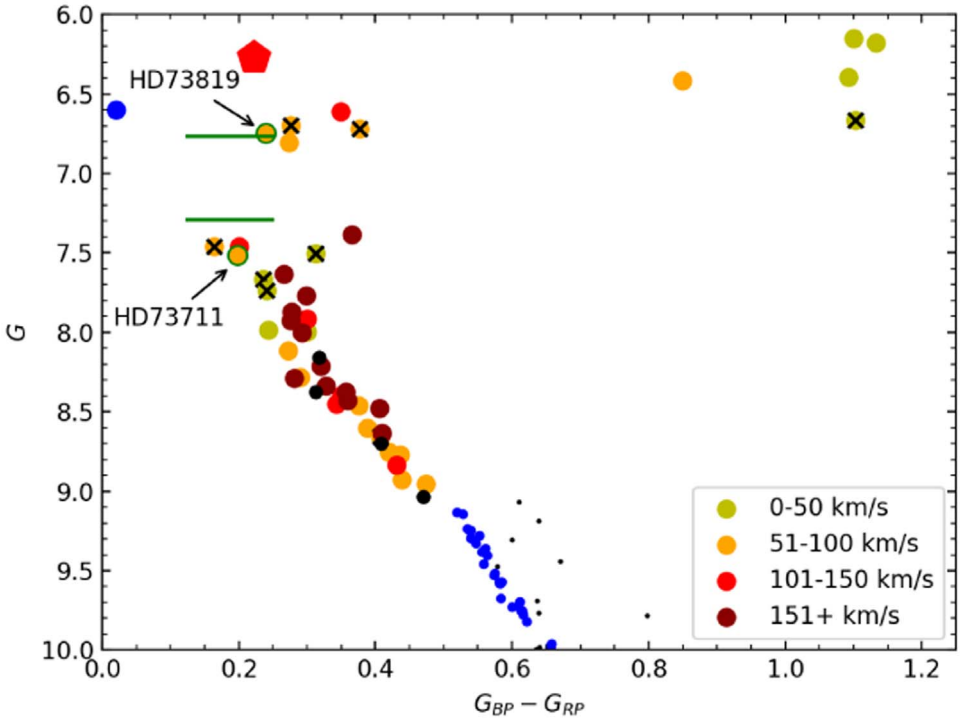


Figure 3. Gaia EDR3 CMD for bright Praesepe members. ϵ Cnc is shown with a large red pentagon, the best-fit main-sequence stars (HD 73819 and HD 73711) are outlined in green, the blue straggler candidate HD 73666 is a large blue point, likely single faint main-sequence stars are small blue points, faint binary candidates are small black points, and stars without measured rotational velocities are large black points. Otherwise the bright stars are color-coded by rotational velocity. Crosses indicate binary systems. The green horizontal lines are inferred brightnesses for ϵ Cnc A and B.

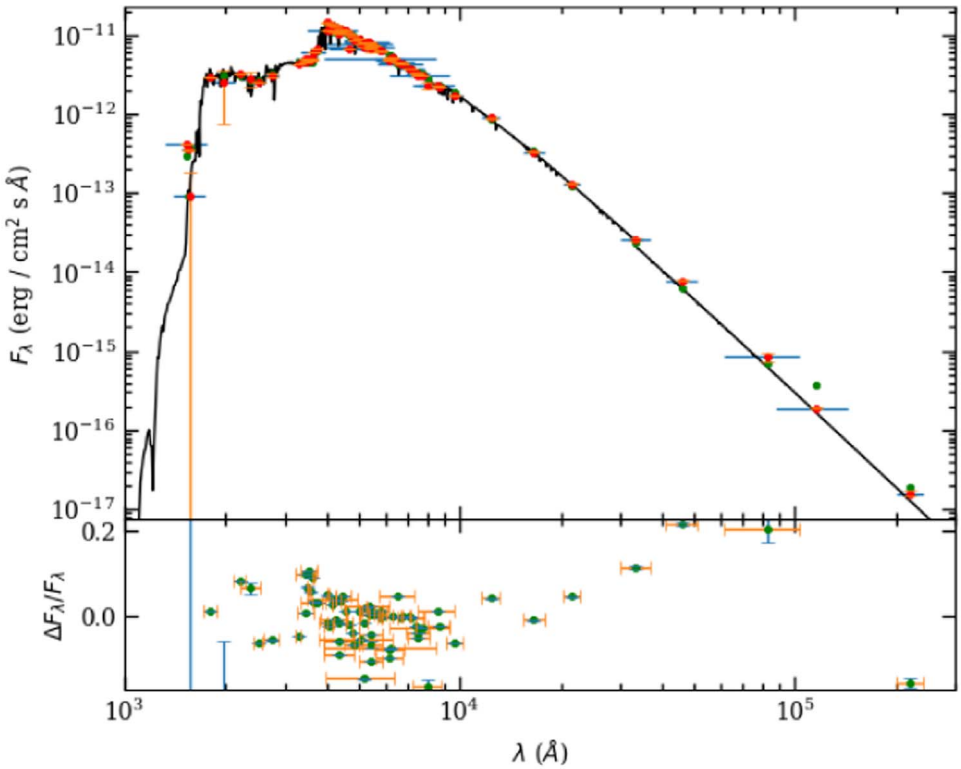


Figure 4. Top: SED for HD 73819 from photometry (red points), compared to an ATLAS9 model with $T_{\rm eff} = 8060$ K and $\log g = 3.6$ and synthetic photometry calculated from the model (green points). Horizontal error bars represent the effective width of the filter. Bottom: fractional difference between the observed photometry fluxes and best-fit synthetic photometry.

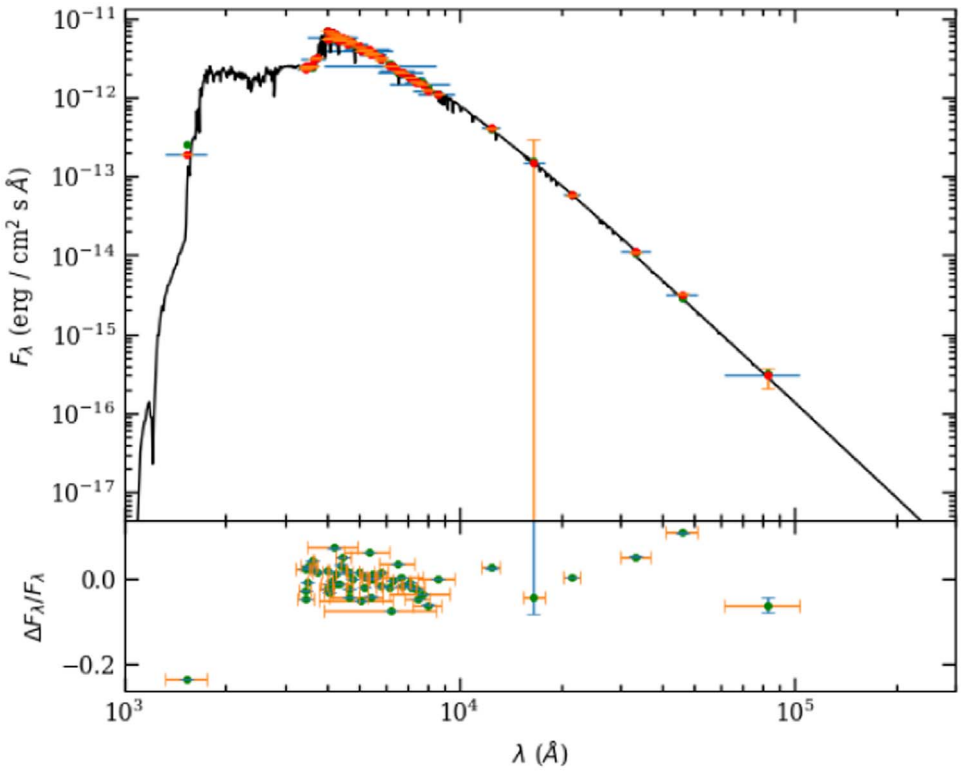


Figure 5. Top: SED for HD 73711 from photometry (red points), compared to an ATLAS9 model with $T_{\rm eff} = 8330$ K and $\log g = 4.0$ and synthetic photometry calculated from the model (green points). Horizontal error bars represent the effective width of the filter. Bottom: fractional difference between the observed photometry fluxes and best-fit synthetic photometry.

of the Balmer jump. The best-fit temperature (8060 K) was chosen based on the minimization of trends in the fractional residuals (bottom panel) as a function of wavelength. The fit returns a bolometric flux $F_{\rm bol} = 5.39 \times 10^{-8}$ erg cm^{-2} s^{-1} when corrected for wavelength-dependent reddening using the relations from Cardelli et al. (1989). At the distance of Praesepe, this corresponds to a luminosity $L = 59.8\ L_\odot$. These values are likely to be fairly good representations of ϵ Cnc A because HD 73819's G magnitude is a good match for the prediction from the spectroscopic luminosity ratio and because the SED of ϵ Cnc is well matched with HD 73819's SED (and it is the biggest contributor to the SED). There are likely to be systematic uncertainties involved, and for this reason, we do not quote uncertainties on these values.

For ϵ Cnc B, we fit the photometric SED of HD 73711 with ATLAS9 models fixing the values [Fe/H] $= +0.2$ and $\log g = 4.0$, as shown in Figure 5. The star has less ultraviolet data, but the optical part of the spectrum is still well sampled. The best-fit temperature was approximately 8330 K, with bolometric flux $F_{\rm bol} = 2.73 \times 10^{-8}$ erg cm^{-2} s^{-1}. At Praesepe's distance, this corresponds to luminosity $L = 30.3\ L_\odot$. In this case, the luminosity is likely to be a significant underestimation of the luminosity of ϵ Cnc B based on the spectroscopic luminosity ratio. Scaling the SED of HD 73711 upward by 10% in all bands improves the matching of the ϵ Cnc SED when added with that of HD 73819.

Using the bolometric fluxes and effective temperatures, we estimate the angular diameters of the two stars using $\theta^2/4 = F_{\rm bol}/\sigma T_{\rm eff}^4$. We find $\theta_1 = 0.194$ mas (from the data for HD 73819) and $\theta_2 = 0.136$ mas (from the data for HD 73711, including the 10% flux correction).

3. Binary Star Modeling

With the observational data in hand, the next task is to fit the orbit of ϵ Cnc and determine its parameters. As a first step, we conducted fits to the radial velocity data alone, partly to derive more realistic a posteriori measurement uncertainties using scatter around the best-fit models and partly to look at velocity offsets between data sets. We used the Eclipsing Light Curve (ELC) code (Orosz & Hauschildt 2000) to fit 11 parameters: period P, reference time of a periastron passage t_P, orbit velocity amplitude of the primary star K_1, mass ratio $q = M_2/M_1$, eccentricity e, argument of periastron ω_1, and system velocities γ_i for five different subsets of data (velocities from KPNO, OHP, and NOT spectra, and literature velocities from Abt & Willmarth 1999 and Abt 1970). Based on the initial fit using a priori measurement errors, we scaled the uncertainties on each velocity data set to return a reduced χ^2 value of approximately 1, and then we refitted. These results are reported in Table 3. The system velocities were in reasonable agreement, but there appeared to be significant offsets that we then corrected for before the joint interferometry−spectroscopy fitting. (The NOT zero-point was used as the reference.) We find $\Delta\gamma({\rm KPNO} - {\rm NOT}) = -1.32 \pm 0.08$ km s^{-1}, $\Delta\gamma({\rm OHP} - {\rm NOT}) = -0.48 \pm 0.15$ km s^{-1}, $\Delta\gamma({\rm MWO} - {\rm NOT}) = -0.34 \pm 1.09$ km s^{-1}, and $\Delta\gamma$ (A&W99 − NOT) $= -2.06 \pm 0.15$ km s^{-1}.

For the fits to the combined radial velocity and interferometry (visibility amplitudes and closure phases) data set, we developed a program, which we call *interfRVorbit*. In this case, we use a set of 13 parameters to model the orbits: period P, reference time of a periastron passage t_P, orbit velocity amplitudes of both stars K_1 and K_2, systemic velocities for both stars γ_1 and γ_2, eccentricity e, argument of periastron ω,

Table 3
Orbit Fitting Results for ϵ Cnc

Parameter	Interf. and RVs (Equal L Ratios)	σ	RVs Only	σ	A&W99	σ
P (days)	35.14101	0.00005	35.14113	0.00012	35.202	0.033
t_P − 2,400,000	48314.598	0.016	48314.56	0.04	48313.5	0.7
γ_1 (km s^{-1})	34.71	0.03	34.78[a]	0.07	29.9	1.1
K_1 (km s^{-1})	56.60	0.03	56.53	0.08	53.0	1.9
K_2 (km s^{-1})	61.55	0.10	61.50	0.08	67.8	3.9
$q = M_2/M_1$	0.9196	0.0015	0.9192	0.0005	0.78[b]	
e	0.4195	0.0003	0.4165	0.0021	0.32	0.04
ω_1 (deg)	258.38	0.02	258.0	0.2	265	5
γ_2 (km s^{-1})	34.88	0.09				
Ω (deg)	356.069	0.014				
i (deg)	81.454	0.010				
$L_2/L_1(H)$	0.61200	0.0007				
a (mas)	1.9127	0.0004 (0.0047[c])				
$M_1/M_\odot$	2.420	0.008				
$M_2/M_\odot$	2.226	0.004				

Notes.
[a] Value derived from measured Abt & Willmarth (1999) spectra.
[b] The published value in Abt & Willmarth (1999) does not follow from their measured K_1 and K_2, and we recalculate it here.
[c] Systematic error due to absolute wavelength calibration uncertainty for the MIRC-X instrument (Monnier et al. 2012).

argument of the ascending node Ω, inclination i, angular size of the binary semimajor axis a, and brightness ratios in H and K_s bands. The interferometric observations do not have much leverage on the unresolved angular diameters of the stars θ_1 and θ_2, and so we fix these at the values calculated from the SEDs (in the previous section). Observable quantities are then calculated from these parameters through a forward model. In the case of the interferometry, the complex visibility for a uniform disk of angular diameter θ is

$$V = \frac{2J_1(\pi B\theta/\lambda)}{\pi B\theta/\lambda},$$

where J_1 is the first-order Bessel function and B is the projected baseline of the interferometer at the star's sky position. For a binary system, the observable squared visibility is calculated from

$$V^2 = \frac{V_1^2 + r^2V_2^2 + 2|V_1||V_2|\, r\cos[2\pi \boldsymbol{B}\cdot\boldsymbol{s}/\lambda]}{(1+r)^2},$$

where V_1 and V_2 are the complex visibilities of the individual stars, r is the luminosity ratio in the observed band, $\boldsymbol{s}$ is the vector of the angular separation of the two stars on the sky, and $\boldsymbol{B}$ is the baseline vector for the interferometer. For the fits, we have assumed uniformly illuminated disks for both stars and used a single luminosity ratio for all observations within a bandpass (in our case, H or K_s). Bandpasses are broken into smaller parts ($n = \mathrm{int}(200\Delta\lambda/\lambda)$, with $n \geqslant 2$), and the calculated visibilities are averaged,

$$V^2_{\mathrm{band}} = \frac{1}{n}\sum_{i=1}^{n} V_i^2.$$

The closure phase can be calculated as the product of the complex visibilities V measured by each pair of telescopes around a closed triangle of baselines. All of the interferometric astrometry measurements are referenced to the brighter star in the binary, so proper motion does not play any role in the fits.

We search the parameter space using a genetic algorithm (Charbonneau 1995). The goodness of the fit is based on the total χ^2 value from comparing model predictions to observed data. After an initial optimization to find a best fit using a priori measurement uncertainties, we scaled the uncertainties for each observational data set (interferometric visibilities, closure phases, and radial velocities separated by measured star and spectroscopic source) to return a reduced χ^2 of approximately 1. In this way, we make the data point uncertainties consistent with the observed scatter around the best-fit model and attempt to produce appropriate weightings for the different data types in subsequent fits.

We subsequently conducted a 20,000-generation run (with approximately 100 model members per generation) to seek the best-fit model and to derive the parameter uncertainties from trial models near the minimum. The best-fit parameters are given in Table 3, where the spectroscopic orbit from Abt & Willmarth (1999) is also provided for comparison. Uncertainty estimates were generated from the full parameter range covered by models with χ^2 within 1 of the minimum (Avni 1976).

Figure 6 compares the radial velocity measurements with the best-fit model as a function of orbital phase. The eccentricities of the orbits are clearly seen. Although we allowed the systematic velocities for the two stars to be different to account for differences in gravitational redshifts or convective blueshifts between the two stars, the velocities disagree by only about 0.2 km s^{-1}.

The best-fitting model of the binary system's orbit on the sky is shown in Figure 7. Although we specifically fit interferometric observables (fringe visibilities and closure phases), in the figure we show relative position measurements for the epochs when they could be derived. These position measurements are given in Table 4 and were computed using a binary grid search procedure.[13] The position uncertainties include 0.5% uncertainty in the MIRC-X wavelength scale

[13] https://www.chara.gsu.edu/analysis-software/binary-grid-search; Schaefer et al. (2016).

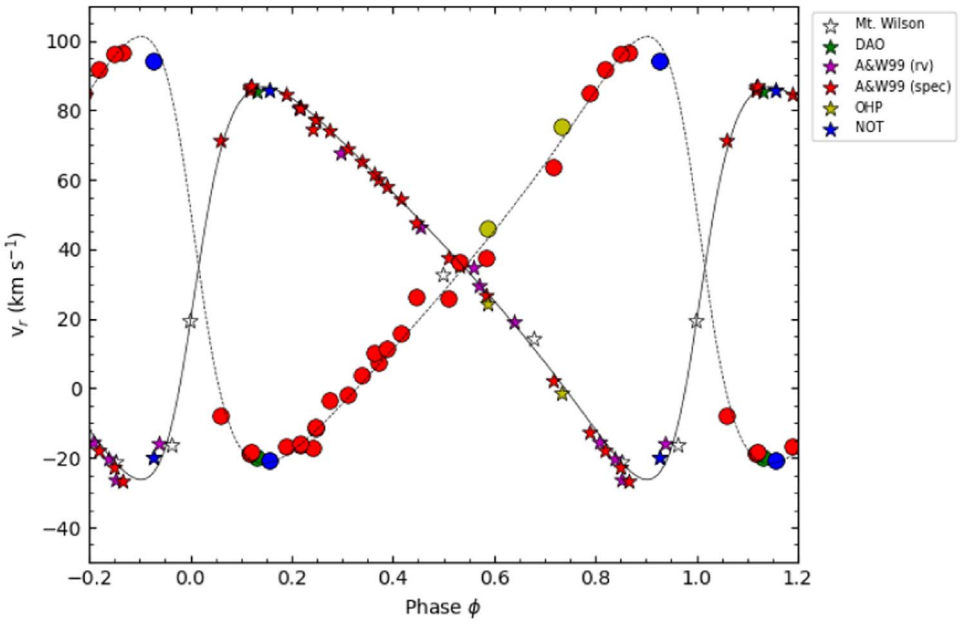


Figure 6. Radial velocity vs. orbital phase for the components of ϵ Cnc. Star symbols represent the primary star, and circles represent the secondary star.

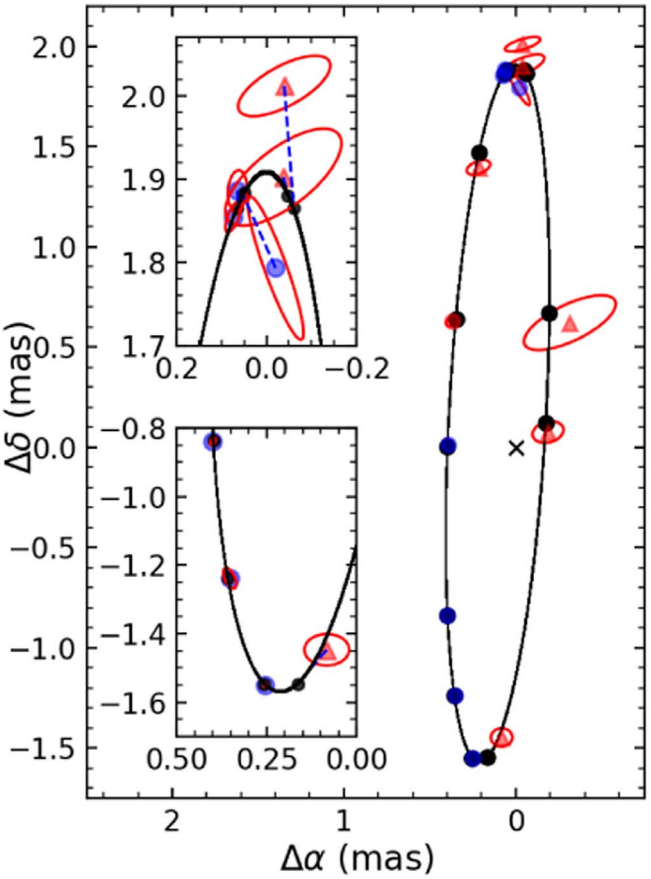


Figure 7. Sky orbit for ϵ Cnc B relative to ϵ Cnc A (marked with a cross). Black points mark the model orbital position during the measurements with the CLIMB beam combiner at CHARA. Blue points are position measurements from the MIRC-X beam combiner. Red points are position measurements from the CLIMB beam combiner (triangles are values closest to the predicted position, and not the global best binary fit). Red ellipses show 5σ uncertainties. Secondary star motion is counterclockwise in this diagram. The inset panels are zoom-ins on observations taken near the extremes of the orbit. In the insets, blue dashed lines connect the measured position to the model's predicted position.

(Anugu et al. 2020). These position measurements are given in Table 4. The comparisons between interferometric observables and model predictions are shown in Figures 8, 9, and 10. For perspective, the closure phases will be near zero (or 180°) for point-symmetric sources, but the maximum excursions away from zero are good indicators of the luminosity ratio of the stars in the binary. (Larger deviations reflect luminosity ratios closer to 1.)

When we allow the *H*- and *K*-band luminosity ratios to be fit independently, the ratios are in rough agreement but differ significantly. Because both filters sample the long-wavelength side of the SEDs of these hot stars, it is to be expected that the ratios would be nearly identical. We therefore conducted a second fitting run where we forced the *H* and *K* luminosity ratios to be the same. Predictably, the final ratio came out very close to the previous *H* ratio owing to the much greater number of interferometric data in that band. It does also lead to a slight shift in the fitted orbit, however, because the choice affects the observational limits from the CLIMB data.

The masses of the primary and secondary stars were computed from the orbital parameters for each run, and we compute 1σ uncertainties on the masses using the range of masses producing χ^2 values within 1 of the minimum value.

Using the period P, orbit velocity amplitudes K_1 and K_2, and inclination i from Table 3, we can calculate the true semimajor axis of the orbit. Used along with the angular size, we get a distance of $183.1 \pm 0.2 \pm 0.5$ pc. (The second quoted error is systematic, deriving from uncertainty in absolute wavelength calibration of the MIRC-X instrument.) This is in good agreement with the geometric distance calculated using the Gaia EDR3 parallax for ϵ Cnc ($d = 184.4^{+1.8}_{-1.4}$ pc; Bailer-Jones et al. 2021).

4. Discussion

We can now use the estimated photometric characteristics of the stars of ϵ Cnc, along with the interferometrically measured masses and radii, to compare with models. One goal of these comparisons is to derive an age as accurate as possible for the

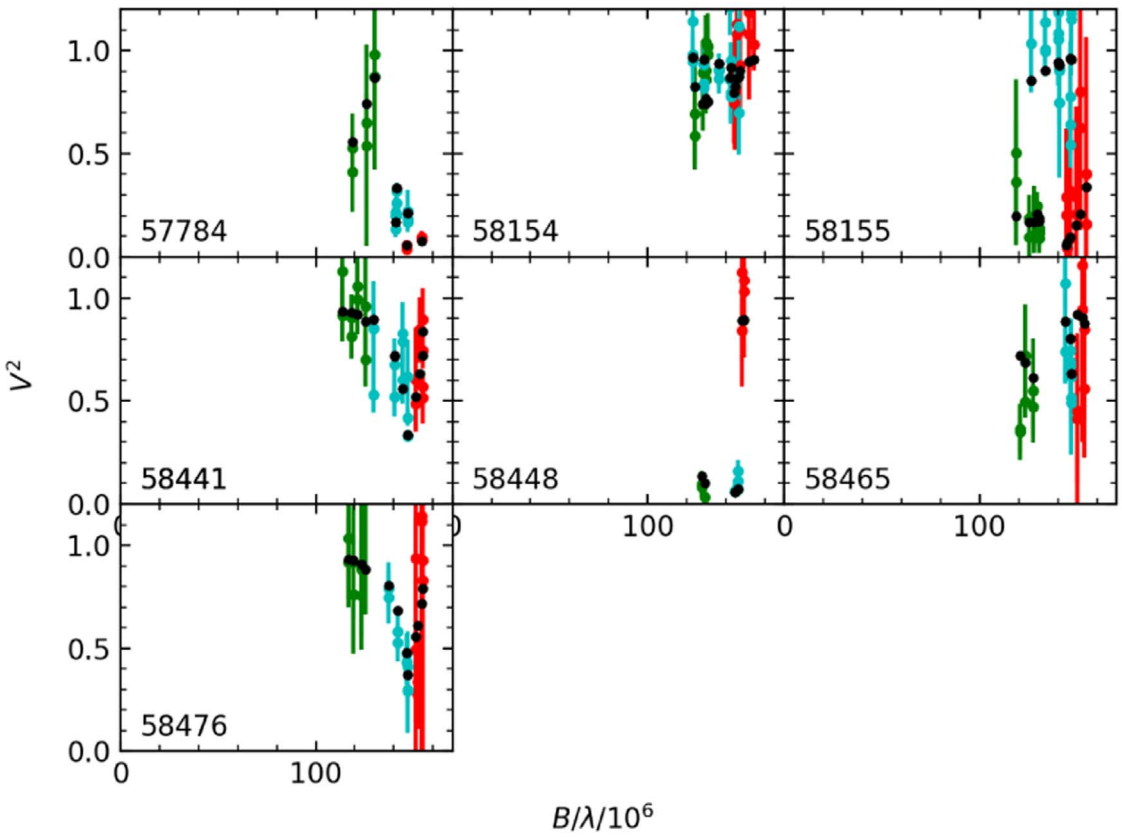


Figure 8. Squared visibilities as a function of interferometric baseline for the CLIMB data, separated by date of observation. Black circles are the predicted values, and the colored circles are the observed values. Different colors in the panels represent measurements from different telescope pairs.

Table 4
Interferometric Relative Position Measurements for ϵ Cnc

mJD[a]	ρ (mas)	θ (deg)	σ_{maj}[b] (mas)	σ_{min}[b] (mas)	φ[b] (deg)	f $L_1/(L_1+L_2)$	σ_f
			CLIMB Combiner[c]				
57784.826	0.7313	30.61	0.0138	0.0091	151.5	0.619	0.008
58154.878	0.2027	292.23	0.0364	0.0208	169.4	0.620[d]	
58155.860	0.6974	333.17	0.1142	0.0372	158.4	0.619	0.122
58441.988	1.9026	358.87	0.0543	0.0159	160.9	0.620[d]	
58448.033	1.4136	8.84	0.0283	0.0125	163.5	0.620[d]	
58465.939	1.4492	176.73	0.0249	0.0183	179.3	0.620[d]	
58476.882	2.0120	358.87	0.0422	0.0104	165.7	0.620[d]	
			MIRC-X Combiner				
58795.986	1.8559	2.28	0.0093	0.0041	132.3	0.613	0.001
58796.057	1.7933	359.35	0.0414	0.0087	55.1	0.572	0.052
58830.984	1.8869	1.96	0.0101	0.0082	112.3	0.617	0.008
59269.783	1.2874	164.14	0.0129	0.0057	66.2	0.617	0.012
59298.759	0.3933	87.66	0.0129	0.0085	46.6	0.641	0.021
59302.695	0.9283	154.57	0.0048	0.0023	113.6	0.617	0.002
59307.677	1.5710	170.74	0.0022	0.0011	138.5	0.608	0.011

Notes.
[a] mJD = HJD −2,400,000.
[b] The size of the error ellipse major and minor axes, and the orientation φ of the major axis relative to north.
[c] CLIMB entries give the binary fit positions most consistent with the orbit.
[d] Luminosity ratio was assumed on nights when the interferometry did not give a reliable independent measurement.

cluster, but we must be wary of the possibility of physics errors in the modeling codes that introduce systematic errors into derived ages. As a result, it is important to examine the cluster stars more broadly in order to validate the coded physics. For our purposes, the treatment of convective cores is critical, as the extent of the core in a star directly determines the amount of fuel available for the main-sequence phase. The masses for both stars in ϵ Cnc put them in the plateau of the amount of

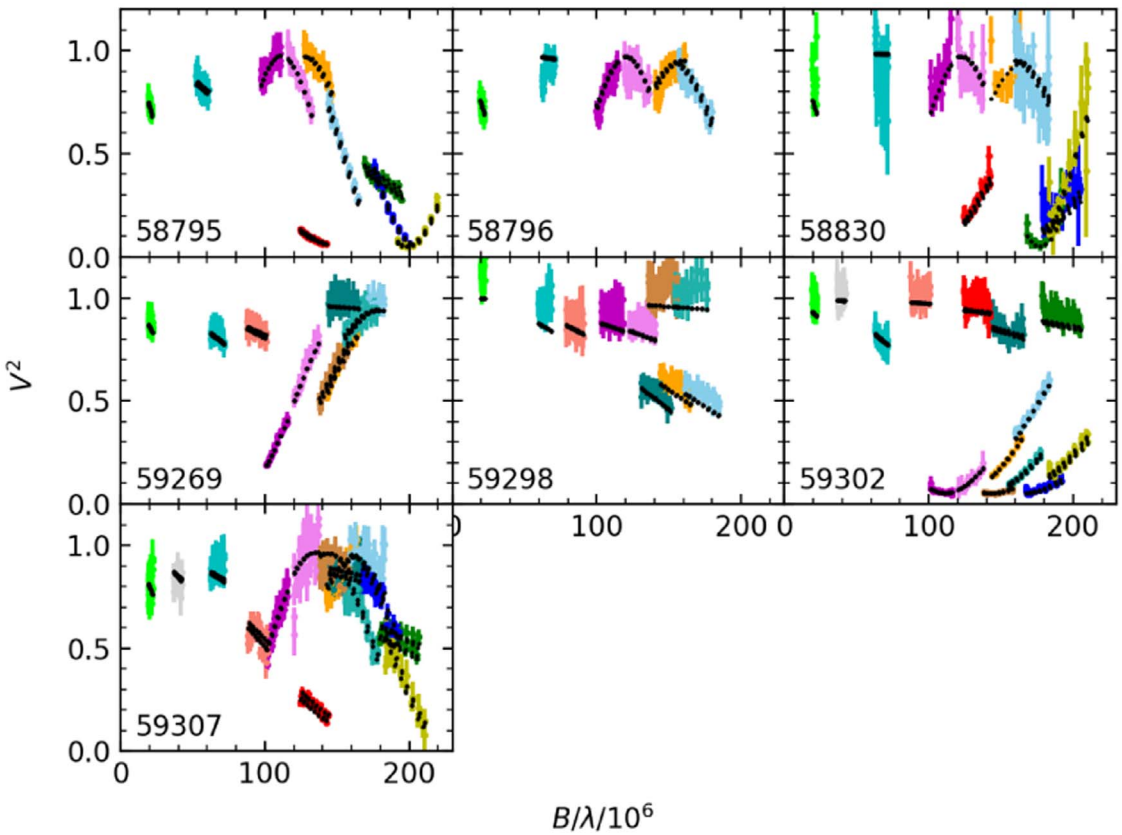


Figure 9. Squared visibilities as a function of interferometric baseline for the MIRC-X data, separated by date of observation. Black circles are the predicted values, and the colored circles are the observed values. Different colors in the panels represent measurements from different telescope pairs.

convective core overshooting embedded into codes, where a fixed overshooting distance (often in terms of pressure scale height H_P) is implemented. At lower masses (usually less than 2 $M_\odot$), a "ramp" is enforced in which the amount of core overshooting is decreased linearly with decreasing mass down to zero for stars that no longer have convective cores. So, in principle, the stars of ϵ Cnc avoid uncertainties related to the implementation of the ramp, but they remain a tough test of convective overshooting because they are stars with precise masses at or near the end of their main-sequence lives, where the convective core history produces its most noticeable effects.

In Table 5, we summarize photometry, rotational velocity, and multiplicity information for the brightest stars in Praesepe. We primarily used Gaia EDR3 information on parallaxes, positions, and proper motions to construct a likely member list. We selected stars based on a position within 5° of $(\alpha, \delta) = (130.10, 19.667)$, a proper-motion vector within 6 mas yr^{-1} of $(\mu_\alpha, \mu_\delta) = (-36.047, -12.917)$, and a parallax within 0.4 mas of 5.371 mas (Gaia Collaboration et al. 2018). Because there is evidence of tidal tails stretching much farther from the cluster center, we examined the membership list of Röser & Schilbach (2019) for additional bright members. While Röser & Schilbach do identify some bright high-probability members in the tidal tails, we find that nearly all of them have radial velocities inconsistent with cluster membership (deviating from the cluster mean by 10 km s^{-1} or more). All of the stars in the table have systematic radial velocities within 5 km s^{-1} of the cluster mean (Raboud & Mermilliod 1998; Abt & Willmarth 1999; de Bruijne & Eilers 2012; Yang et al. 2015; Cummings et al. 2017).

Figures 11–13 show comparisons between theoretical isochrones and Gaia photometry for the cluster. In Figures 11 and 12, evolution tracks for the measured masses of the ϵ Cnc stars are shown on top of the isochrones. Our most important limits come from the luminosity ratios and the total photometry for the binary. While metallicity affects the luminosity of the stars in the last stages of core hydrogen burning (in the sense that more metal-poor models are more luminous), the amount of convective core overshooting appears to be an important factor in the models shown here. PARSEC models have the largest amount of core overshooting ($\sim 0.25 H_P$ for $M > 1.5\ M_\odot$) among the models examined here, and the predicted luminosities of the ϵ Cnc components appear to be too high to reproduce ϵ Cnc. (Alternately, if the luminosities are forced to match the observations, the primary star is forced to be too red, and the color of the binary cannot be matched.) The MIST and BaSTI-IAC evolution tracks for the masses of the ϵ Cnc components pass through the observed magnitude levels toward the end of core hydrogen burning, which occur near the red kinks in each track. The redward end of the kink approximately matches the CMD positions of the bright single main-sequence stars in Praesepe as well. As shown in Figure 14, MIST models match the inferred G magnitudes of both components to within the uncertainties in the range 632–641 Myr if the masses are as measured and the cluster metallicity roughly matches the value from the literature ([Fe/H] = +0.14). When the model photometry values are combined, the measured Gaia photometry for the system is also matched.

Uncertainties on the measured masses and cluster metallicity extend the range of acceptable ages. Lower primary star masses

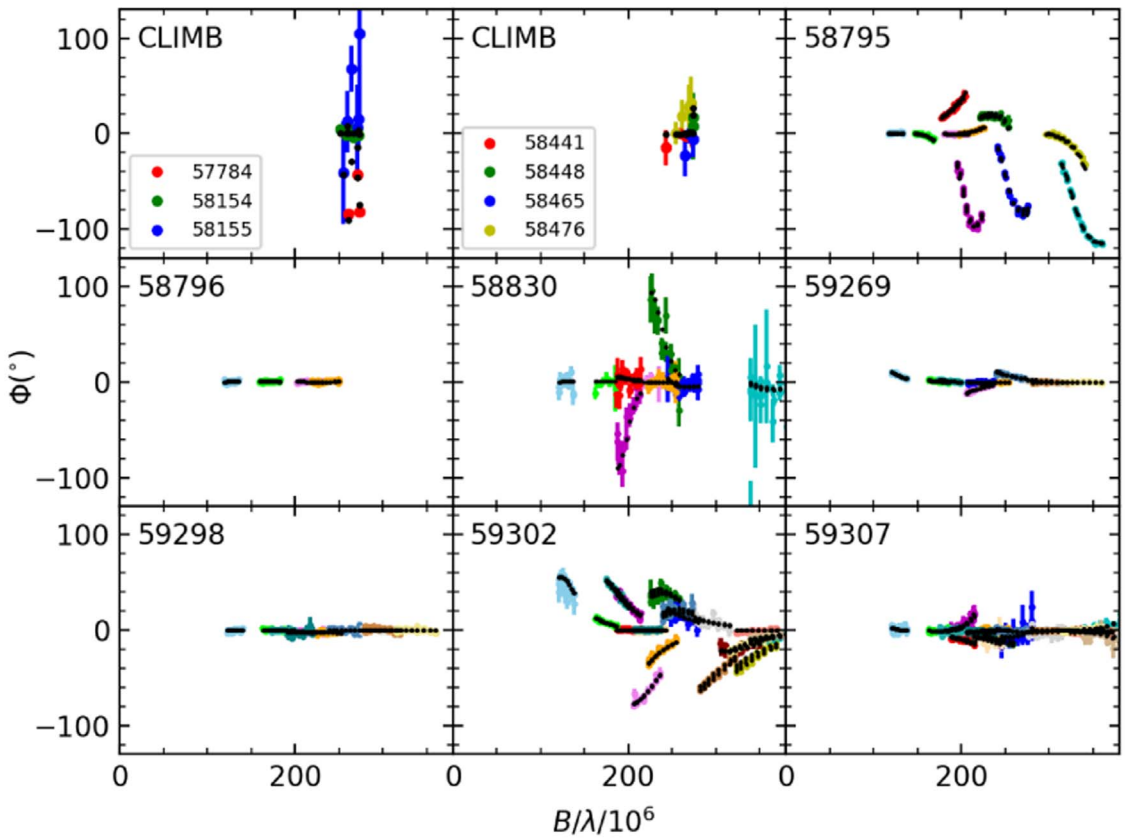


Figure 10. Closure phases (Φ) as a function of the interferometric baseline for CLIMB and MIRC-X data, separated by date of observation. Here the baseline is the sum of the baseline lengths for the first two legs of the triangle of telescopes. Black circles are the predicted values, and colored circles are observed values on different dates (CLIMB) or from different telescope pairs (MIRC-X).

and higher-metallicity models require older ages. The primary star mass uncertainty results in about 15 Myr of age uncertainty. At the ends of the mass and metallicity uncertainty ranges, color changes in the primary star lead to unsatisfactory matches to the observed color of the binary. This is a stronger effect for the metallicity, with [Fe/H] values more than about ± 0.03 dex (approximately 0.5σ) away from the spectroscopic value producing stellar colors that are too blue or red. A 0.5σ uncertainty in metallicity results in an age uncertainty of about 10 Myr. Adding these uncertainties in quadrature, we therefore quote an age uncertainty of 19 Myr. Perhaps more importantly than the statistical uncertainty, we believe that the observational limits reduce systematic errors in the age by ruling out some isochrone sets (and the model physics they utilize) as unable to reproduce the characteristics of ϵ Cnc. Smaller changes to the amount of convective core overshooting could still produce model stars consistent with the characteristics of the components of ϵ Cnc at different ages (with larger amounts of overshooting resulting in younger ages). We also note that the initial He abundance of these metal-rich Praesepe stars carries some uncertainties that affect the detailed comparisons with models, including the color of the main sequence and the main-sequence lifetime of turnoff stars (for a discussion of this issue in the even more metal-rich cluster NGC 6791, see Brogaard et al. 2011, 2012). Evaluation of these contributions to the age uncertainty is beyond the scope of this study, however.

An MIST isochrone of approximately 635 Myr and the spectroscopically measured cluster metallicity can simultaneously match the blue edge of the distribution of bright main-sequence stars, the red extent of the red kink at the cluster turnoff, and the magnitudes of the components of ϵ Cnc at their measured masses.

While it is gratifying that models reproduce several important features of the CMD, a careful examination raises some questions. The isochrone does not match the photometry of the star HD 72779 in the Hertzsprung gap. (See Appendix A.1 for evidence that the star is single and representative of where the subgiant portion of the isochrones should be.) This may indicate some mismatch in the hydrogen abundance profile near the core at hydrogen exhaustion. The distribution of stars in the range $6.5 < G < 7.5$ is also difficult to interpret with conventional stellar models (Figures 11–13). The stars at $G \approx 6.7$ and 7.5 are consistent with a single age of around 635 Myr, with the first group of stars at the turnoff and the second group near the reddest point in the isochrone's kink (Figure 11). According to the evolutionary timescales, both parts of the isochrone should be fairly well populated. However, the range $6.8 < G < 7.4$ should also be occupied, as it should still contain stars burning core hydrogen, and we find no stars in this range. Additionally, most of the bright main-sequence stars in Praesepe ($7.5 < G < 10$, $1.2 < M_G < 3.7$) reside brighter or redder than the model isochrones, although the amount of disagreement varies between model sets and can be affected by chemical composition (metallicity or He abundance). In addition, there appears to be a jag in Praesepe main sequence at $G \approx 9.1$ ($M_G \approx 2.8$), and slightly fainter stars seem to deviate noticeably from the models. An examination of the Hyades (below) does not give us clear evidence for a similar feature. The Praesepe

Table 5
Rotational Velocities and Multiplicity of Bright Stars ($G < 9.0$) in Praesepe

KW	HD/BD	G	$v \sin i$ (km s^{-1})	References	Multiplicity	References	Notes
253	73665	6.15	<10	3	No	3,14	RC
283	73710	6.18	<10	3	No	3,14,15	RC
212	73598	6.39	<10	3	speck,occ	14,16	RGB?
	72779	6.42	99	3	No	3,14	SGB
428	73974	6.66	<10	3	SB1O,occ	3,15	SGB
265	73666	6.58	9/10	3,5	No/occ	3/14	BSS
204	73575	6.61	150/129/127/140	1,3,5,11	No	3,14,15,16	δ Sct
50	73210	6.70	80/90/90,80	1,2,3	SB2O	3	
284	73712	6.72	56:,61:	3	SB2O	3,14,16	δ Sct, triple?
348	73819	6.74	152/180/79	1,3,11	No	3,14,15,16	δ Sct
328	73785	6.80	85/91	1,3	No/SB2?	3,15,16/7	
150	73449	7.38	235/229	1,3	No/SB?	3,14,15/7	δ Sct
534	72942	7.46	62/73	1,5	SB1O	3	A/Am hybrid
	72846	7.46	119 ± 6	6	No?	14	
229	73619	7.50	$20,18/11.2 \pm 0.5$	3,4	SB2O	3,7	Am
276	73711	7.52	$60/66/66 \pm 11/62$	1,3,4,5	No/SB2?	3,14,15/7,9	Am
207	73576	7.63	$200/204/208 \pm 11$	1,3,10	No/SB1?	3,14/7	δ Sct
279	73709	7.67	$20/17.3 \pm 0.3/10$	3,4,5	SB1O	3,7	quadruple,Am
40	73174	7.74	$11/7.3 \pm 1.1/<5$	3,4,5	SB1O,SB1O	3	triple,Am
323	73763	7.77	200 ± 3	10	No?	14	δ Sct
449	74050	7.86	$150/188 \pm 8/145$	1,6,11	No?	14	δ Sct
445	74028	7.92	$160/150 \pm 9$	1,6	No?	14,15,16	δ Sct
203	73574	7.92	$108/108/102 \pm 4$	1,3,6	No/bin	3/14,15	
286	73730	7.98	$30/34.4 \pm 3.4/29/35$	1,4,5,8	No?	14,15	Am
	74656	7.99	25 ± 1	6	No?	13	Am
385	73890	8.00	165/141	1,11	No?	14	δ Sct
114	73345	8.11	$98/85/85 \pm 4/90$	1,2,6,8	No?	14,15	δ Sct
	74740	8.16			No?	12,13	
45	73175	8.21	$180/163 \pm 9/175$	1,6,8	No?	14	δ Sct
143	73430	8.28	82/73/80	1,5,8	No?/occ	14/15	
375	73872	8.29	180/135	1,8	No?/SB1?	14,15/7	δSct
	74718	8.33	155 ± 7	6	No?	17	
	72757	8.37	179 ± 10	6			
	74720	8.38			speck	18	no rv measure?
	74589	8.40	127 ± 5	6	No?	13	pulsator
340	73798	8.43	$175/200 \pm 11/200$	1,6,8	No?	14	δ Sct
154	73450	8.45	$138/140/138 \pm 7/166$	1,2,6,8	No?	14,15	δ Sct
	74587	8.46	90 ± 4	6	No?	13	δ Sct
429	73993	8.48	$200/240 \pm 14/210$	1,6,8	No?	14	
318	73746	8.60	$110/87/95 \pm 4/95$	1,2,6,8	No?	14	δ Sct
38	73161	8.63	160/190	1,8	No?	14,15	
350	73818	8.65	85/81/66/65	1,4,5,8	SB1	5	Am
	70297	8.70					no rv measure?
271	+20 2161	8.76	85/69/78	1,2,8	No?	14	
	74135	8.77	100 ± 4	6			pulsator
226	73616	8.83	125/110/115	1,2,8	No?	14,15	pulsator
124	73397	8.92	100/86/91	1,2,8	SB1O	7	pulsator
370	73854	8.95	137/68/70	1,2,8	No?	14,15	pulsator
	73620	9.04					

Note. KW identifications are from Klein Wassink (1927).
References. (1) McGee et al. 1967; (2) Rachford 1998; (3) Abt & Willmarth 1999; (4) Debernardi et al. 2000; (5) Fossati et al. 2007; (6) Fossati et al. 2008; (7) Raboud & Mermilliod 1998; (8) Cummings et al. 2017; (9) Burkhart & Coupry 1998; (10) Royer et al. 2002; (11) Bush & Hintz 2008; (12) Evans et al. 1985; (13) Grenier et al. 1999; (14) Mason et al. 1993a; (15) Peterson & White 1984; (16) Peterson et al. 1989; (17) Evans & Edwards 1983; (18) Horch et al. 2017.

feature appears to be about a magnitude too bright to be related to the Kraft break (Kraft 1967) in stellar rotation rates.

The Hyades provides a useful comparison, as it has nearly identical age and chemical composition and a similar richness of stars. Bright Hyades members are plotted in Figure 15, with the plot ranges chosen to cover the ranges in the Praesepe plots. There are no stars found at the luminosity level of the brighter group ($G \approx 6.7$ in Praesepe, $M_G \approx 0.4$), and a handful of stars are scattered above the bright end of the main sequence in Praesepe ($G \approx 7.5$, $M_G \approx 1.2$). Most of these bright stars have shown some evidence of binarity in the literature, but we discuss in Appendix A.2 why we believe that the photometry for most of the stars with $M_G < 1.6$ and $(G_{BP} - G_{RP}) < 0.3$ is probably representative of single stars. Similarly to the

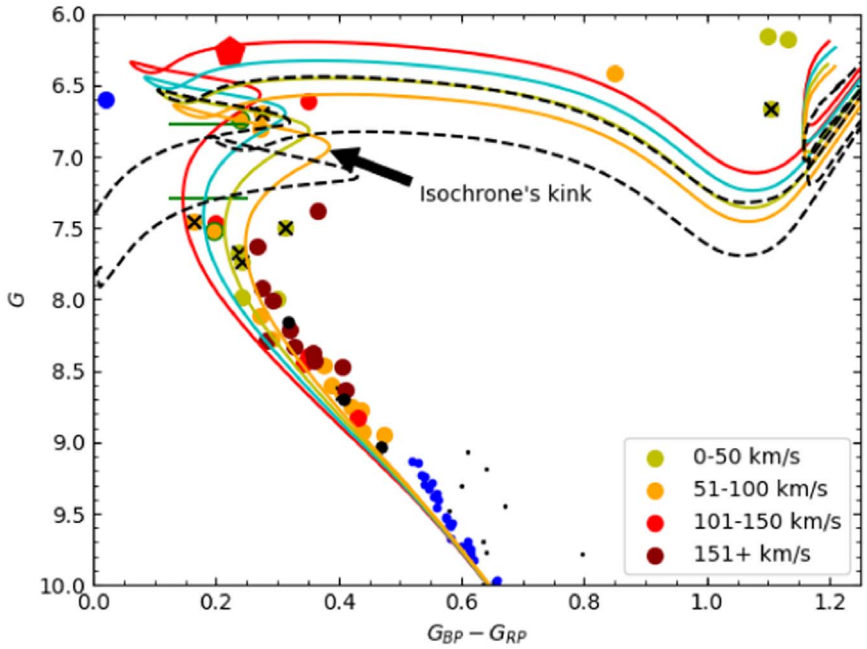


Figure 11. MIST isochrones (Choi et al. 2016) for ages 600 (red), 650 (cyan), 700 (yellow), and 750 (orange) Myr. MIST evolutionary tracks are also shown (black) for masses of the primary and secondary star ($M_p = 2.420\ M_\odot$, $M_s = 2.226\ M_\odot$). Crosses indicate binary systems. To graph the evolution tracks and isochrones, a distance modulus $(m - M)_0 = 6.33$, initial rotation $v/v_{\rm crit} = 0$, iron abundance [Fe/H] = +0.16, and reddening $E(G_{\rm BP} - G_{\rm RP}) = 0.073$ were used.

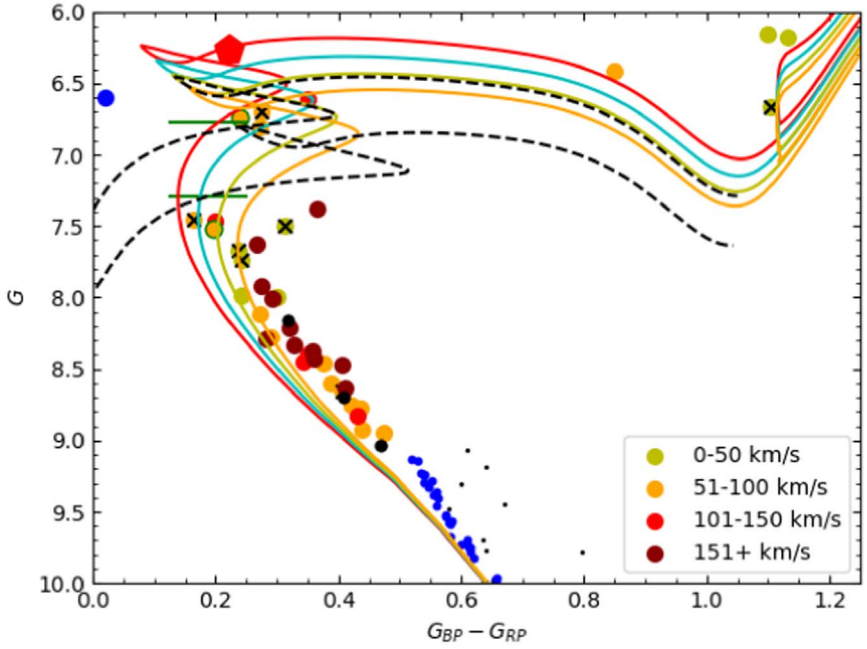


Figure 12. BaSTI-IAC isochrones (Hidalgo et al. 2018) for ages 600 (red), 650 (cyan), 700 (yellow), and 750 (orange) Myr. BaSTI-IAC evolutionary tracks are also shown (black) for masses of the primary and secondary stars ($M_p = 2.420\ M_\odot$, $M_s = 2.226\ M_\odot$). Crosses indicate binary systems. In the graph, distance modulus $(m - M)_0 = 6.33$, iron abundance [Fe/H] = +0.16, and reddening $E(G_{\rm BP} - G_{\rm RP}) = 0.073$ were used. Overshooting and diffusion were also allowed under available grids.

situation for Praesepe, there appear to be almost no stars present in what should be the last stages of core hydrogen burning, between the turnoff and the red kink.

In summary, the component stars of ϵ Cnc and the two groups of late main-sequence stars push for an age around 637 ± 19 Myr, but the single star in the Hertzsprung gap and the gap in the star distribution may imply a statistical fluke or possibly an error in the stellar model physics or chemical composition. In addition, the PARSEC isochrones generally predict too high a luminosity for a star of ϵ Cnc A's mass in the cluster, while the MIST and BaSTI-IAC isochrones reproduce the luminosity better. As a result, we believe that our analysis puts limits on the amount of convective core overshooting used in the isochrones and therefore reduces systematic uncertainties in the cluster age. We encourage work to analyze additional stars in Praesepe in order to identify the cause of these inconsistencies.

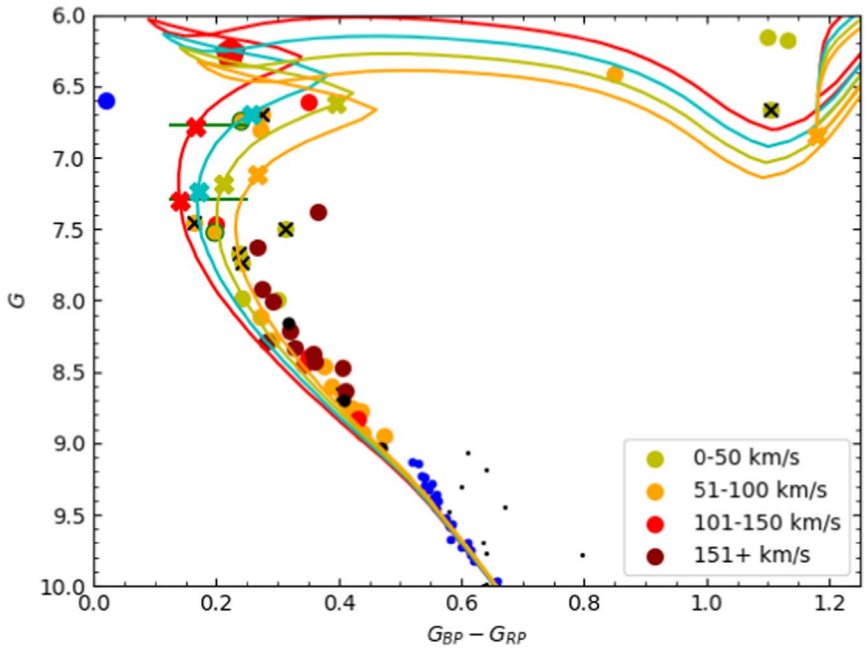


Figure 13. PARSEC isochrones (Bressan et al. 2012) for ages 600 (red), 650 (cyan), 700 (yellow), and 750 (orange) Myr. In the graph, distance modulus $(m - M)_0 = 6.33$, iron abundance [Fe/H] $= +0.16$, and reddening $E(G_{BP} - G_{RP}) = 0.073$ were used. Crosses indicate binary systems. The colored crosses indicate where our calculated masses in Table 3 land on the isochrone.

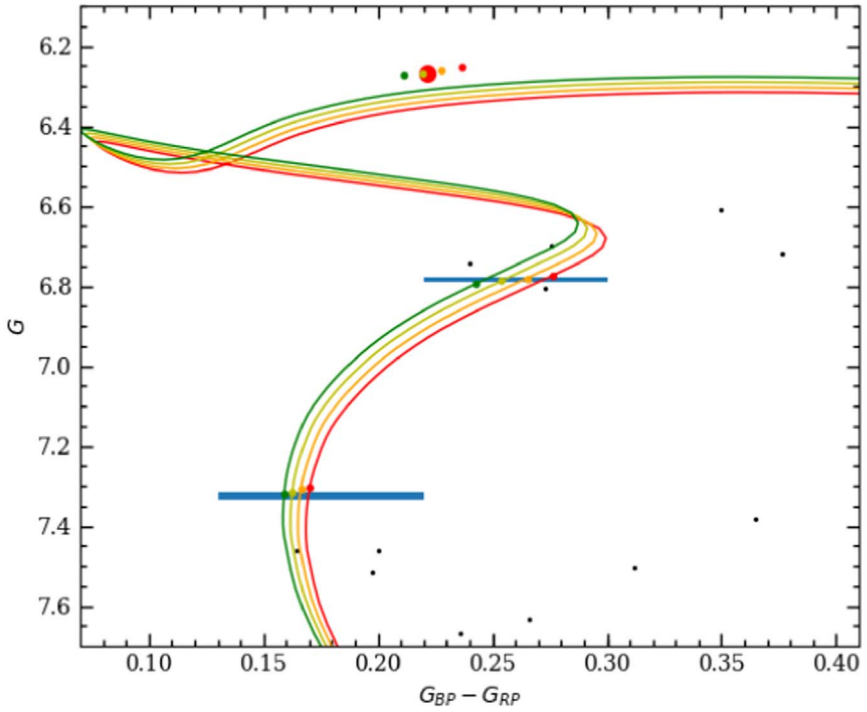


Figure 14. MIST isochrones (Choi et al. 2016) for ages 630 (green), 635 (light green), 640 (yellow), and 645 (orange) Myr. Distance modulus $(m - M)_0 = 6.33$, iron abundance [Fe/H] $= +0.14$, and reddening $E(G_{BP} - G_{RP}) = 0.073$ were used. Colored circles show the model positions of stars with the measured masses of the components of ϵ Cnc, and blue rectangles show the G magnitude and uncertainty of the components as inferred from spectroscopy.

4.1. White Dwarf Progenitor Masses

A primary result of the measurements of ϵ Cnc is the precise measurement of the mass of a star near the end of core hydrogen burning. This significantly reduces the uncertainties in the predicted masses of more evolved stars and more cleanly separates those predicted masses from uncertainties surrounding the cluster age. While there are still some uncertainties surrounding subsequent evolutionary phases, this can improve the determination of WD progenitor masses in the cluster.

For a single-age cluster, Praesepe contains a sizable sample of WDs with measured masses covering a fairly large range from about 0.7 to 0.9 $M_{\odot}$ (Cummings et al. 2018; Salaris & Bedin 2019). These WDs are in a transitional range between the masses of common field WDs with CO compositions and

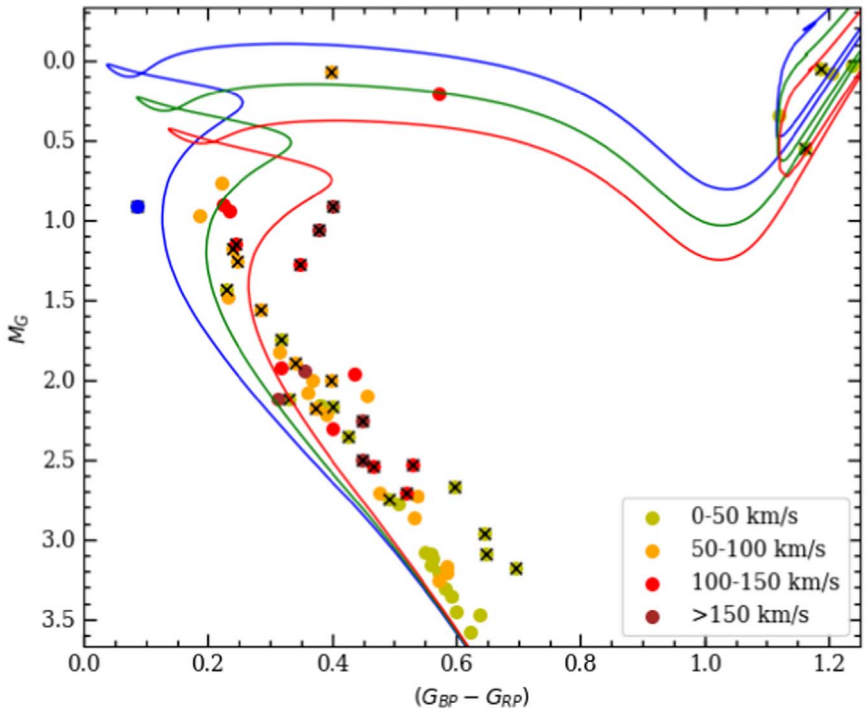


Figure 15. Hyades members in a color–absolute magnitude diagram using Gaia EDR3 photometry and parallaxes. Color-coding for individual stars is based on measured rotational velocity $v_{\rm rot} \sin i$, and crosses indicate binary systems. The blue point is the blue straggler δ^3 Tau. MIST isochrones (Choi et al. 2016) for [Fe/H] = +0.14 and zero reddening are shown, with ages 635 (blue), 740 (green), and 850 (red) Myr shown.

Table 6
Initial Mass Determinations for Praesepe WDs

ID	$M_{\rm WD}/M_\odot$[a]	$t_{\rm cool}$ (Myr)[a]	$M_i/M_\odot$
WD 0833+194	0.813 ± 0.027	364^{+33}_{-30}	$3.71^{+0.19}_{-0.14}$
WD 0836+199	0.830 ± 0.028	352^{+34}_{-31}	$3.66^{+0.19}_{-0.11}$
WD 0837+189	0.870 ± 0.029	402^{+42}_{-39}	$3.92^{+0.29}_{-0.23}$
WD 0837+199	0.757 ± 0.025	190^{+16}_{-15}	$3.16^{+0.06}_{-0.06}$
WD 0840+190	0.895 ± 0.030	425^{+48}_{-44}	$4.07^{+0.43}_{-0.30}$
WD 0840+200	0.752 ± 0.027	233^{+19}_{-18}	$3.27^{+0.07}_{-0.07}$
WD 0843+184	0.898 ± 0.028	423^{+38}_{-41}	$4.05^{+0.32}_{-0.28}$

Notes.
[a] Cummings et al. (2018).

Table 7
Literature Radial Velocity Measurements for ϵ Cnc A

mJD[a]	$v_{r,A}$ (km s^{-1})	σ_v	Phase ϕ	Source
19849.3[b]	17	5	0.971	Potsdam
19852.3[b]	73	5	0.057	Potsdam
23451.941	32.6	9.6	0.489	MWO
23534.651	−21.3	2.5	0.843	MWO
23539.721	19.3	16.9	0.987	MWO
23563.646	14.4	3.5	0.668	MWO
23573.664	−16.4	12.4	0.953	MWO
48309.755	−28.5	3.5	0.853	KPNO
48312.724	−17.9	3.5	0.938	KPNO
48330.863	44.2	3.5	0.454	KPNO
48580.917	27.5	3.5	0.569	KPNO
48673.845	78.3	3.5	0.214	KPNO
48676.736	65.3	3.5	0.296	KPNO
48694.761	−17.6	3.5	0.809	KPNO
48695.800	−22.4	3.5	0.839	KPNO
48969.909	16.9	3.5	0.639	KPNO
49107.740	32.4	7	0.561	KPNO

Notes.
[a] mJD = HJD −2,400,000.
[b] Estimated, as time of observation is not available.

massive WDs above 1 $M_\odot$ presumed to have ONe compositions. The progenitor stars are believed to be ones that ignite helium burning in a nondegenerate core, but they do not experience a second convective dredge-up in their asymptotic giant stage. The second dredge-up limits the growth of the hydrogen-depleted cores in more massive stars and results in slower growth of WD masses with increasing initial star mass. More precise determinations of the initial masses for Praesepe's WDs can produce a strong lower mass limit for stars that undergo the second dredge-up, as well as a stronger test of our understanding of the IFMR in this transition range.

To determine initial masses for these WDs, we started with isochrones for which a star of ϵ Cnc A's mass passed through the range of G magnitudes we limited the star to earlier in this paper. We then subtracted cooling times for the Praesepe WDs from Cummings et al. (2018) from the isochrone ages and calculated isochrones for those younger ages. The progenitor masses for the WDs are then the initial masses of stars ending the asymptotic giant branch at that earlier time. Although the initial masses derived in this way are still somewhat subject to uncertainties in evolutionary phases after the main sequence (most notably during the relatively long core helium burning phase), the progenitor masses are more explicitly tied to masses measured for present-day stars. We based our calculations on PARSEC models exclusively because of the difficulties other isochrone sets had in reproducing the CMD position of ϵ Cnc A, and these difficulties probably result from differences in

Table 8
Radial Velocity Measurements for ϵ Cnc A and B

mJD[a]	$v_{r,A}$ (km s^{-1})	σ_v	$v_{r,B}$ (km s^{-1})	σ_v	Phase ϕ	Source
22384.753	85.4	3	−20.1	3	0.121	DAO
48613.92562	36.5	1.5	24.7	2.8	0.509	KPNO
48638.82381	79.9	1.1	−17.4	2.7	0.217	KPNO
48639.93300	76.3	1.1	−12.5	2.7	0.249	KPNO
48674.83253	73.4	1.0	−18.4	2.9	0.242	KPNO
48696.76600	−27.9	0.6	95.6	2.2	0.866	KPNO
48967.99971	25.5	1.3	36.4	3.0	0.584	KPNO
49019.89793	70.1	1.1	−9.1	2.9	0.061	KPNO
49021.87432	84.6	0.9	−19.9	2.5	0.117	KPNO
49021.93111	85.3	0.9	−19.7	2.4	0.119	KPNO
49021.98021	85.6	1.0	−19.5	2.3	0.120	KPNO
49030.84515	58.7	1.3	6.3	3.7	0.373	KPNO
49080.62158	−13.8	1.1	83.6	2.8	0.789	KPNO
49081.70621	−19.2	1.0	90.5	2.6	0.820	KPNO
49082.71360	−23.8	1.0	94.9	2.8	0.849	KPNO
49094.69748	83.5	1.0	−17.8	2.3	0.190	KPNO
49095.69961	79.4	1.0	−17.1	2.7	0.218	KPNO
49096.69919	76.3	1.1	−12.3	3.0	0.247	KPNO
49097.71513	72.9	1.0	−4.7	3.0	0.276	KPNO
49106.71287	33.8	1.4	35.3	2.7	0.532	KPNO
49344.96554	67.7	1.2	−3.0	3.1	0.311	KPNO
49345.98097	64.2	1.3	2.8	3.2	0.340	KPNO
49381.90408	60.6	0.9	9.0	3.6	0.363	KPNO
49382.80479	56.7	1.4	10.4	3.5	0.388	KPNO
49383.77115	53.2	1.5	14.6	4.1	0.416	KPNO
49384.87950	46.3	1.4	25.2	3.1	0.447	KPNO
50800.02879	1.1	1.3	62.4	3.7	0.717	KPNO
53009.47942	23.9	0.1	45.6	2.2	0.590	OHP
53014.62148	−1.8	0.1	75.0	1.9	0.736	OHP
58960.37513	−19.8	0.1	94.3	1.3	0.931	NOT
58960.37905	−19.8	0.1	94.1	1.3	0.931	NOT
58968.40424	86.1	0.1	−20.4	1.5	0.160	NOT
58968.40826	86.0	0.1	−20.5	1.5	0.160	NOT

Notes.
[a] mJD = HJD −2,400,000.
[b] The normalized digitized spectra for KPNO and NOT (30 spectra) are available as the Data behind the Figure.

(This table is available in its entirety in machine-readable form.)

convective core overshooting algorithms. Based on the new age estimation of 637 ± 19 Myr, the new initial masses are given in Table 6.

In their examination of the IFMR, Cummings et al. (2018) derived ages for Praesepe of 705 ± 25 Myr and 685 ± 25 Myr from nonrotating PARSEC and MIST isochrones, respectively, for [Fe/H] = +0.15 but zero reddening. Salaris & Bedin (2019) used the age derived by Gaia Collaboration et al. (2018): 708^{+140}_{-90} Myr for [Fe/H] = +0.16 and reddening $E(B-V) = 0.027$. Even with high-quality Gaia photometry, there is definite ambiguity in fitting the CMD with isochrones owing to the small number of bright stars and potentially confounding factors like binarity and high rotation rates. Our lower age results in higher initial masses for the cluster WDs by 0.14–0.31 $M_\odot$ relative to the MIST results from Cummings et al. For all but the youngest WDs, the cooling time uncertainty is the largest contributor to the uncertainty in the initial masses. Salaris & Bedin (2019) derived cooling times from fitting tracks to Gaia DR2 photometry of the WDs and found values that were in most cases smaller (by ∼80–160 Myr) than those of Cummings et al. (2018). Cummings et al. derived cooling times from spectroscopic measurements of $T_{\rm eff}$ and $\log g$. As a result, it should be remembered that systematic uncertainties in the cooling times could have a larger effect on the initial masses than our revision of the cluster age.

We believe that our determinations represent an improvement in how realistic the statistical uncertainties are (because Cummings et al. appear to have only included cooling time uncertainties in their quotations of initial mass uncertainties) and in reducing systematic uncertainties (because the measured star masses allow us to identify isochrones that match masses and CMD properties).

5. Conclusion

Our overall goal was to determine the age of the open star cluster Praesepe using the binary star system ϵ Cnc. Using radial velocities and interferometric measurements, we have been able to calculate the primary star's mass as 2.420 ± 0.008 $M_\odot$ and the secondary star's mass as 2.226 ± 0.004 $M_\odot$, as well as put observational limits on the brightness of the two stars. With this information, we find that MIST models with the spectroscopic cluster metallicity are able to successfully reproduce the inferred CMD positions of the stars of ϵ Cnc at their masses and the position of the pre-core hydrogen exhaustion kink. While this gives evidence in favor of the commonly used amount of convective core overshooting in the MIST models, there are other features (the luminosity of a cluster subgiant, and an unusual distribution of stars brighter than the cluster turnoff) that may be indicating issues with model physics that should be investigated further. The MIST models indicate an age of 637 ± 19 Myr for the cluster.

The direct measurement of masses for stars nearing core hydrogen exhaustion also allows us to reexamine the likely progenitor masses for the cluster WDs. Our measurements imply an upward shift to the initial masses for WDs in the 0.7–0.9 $M_\odot$ range, although systematic uncertainties in cooling ages need to be addressed and could have a substantial effect.

We gratefully acknowledge the assistance of Daryl W. Willmarth in locating and providing Kitt Peak spectra of ϵ Cnc from more than 25 yr ago, as well as support from the National Science Foundation under grant AAG 1817217 to E. L.S. This research made use of observations from the SIMBAD database, operated at CDS, Strasbourg, France; the WEBDA database, operated at the Institute for Astronomy of the University of Vienna; and data products from the AAVSO Photometric All-Sky Survey (APASS), funded by the Robert Martin Ayers Sciences Fund and the National Science Foundation (grant AST-1412587). We use observations made with the Nordic Optical Telescope, owned in collaboration by the University of Turku and Aarhus University, and operated jointly by Aarhus University, the University of Turku, and the University of Oslo, representing Denmark, Finland, and Norway, the University of Iceland, and Stockholm University at the Observatorio del Roque de los Muchachos, La Palma, Spain, of the Instituto de Astrofisica de Canarias.

This work is based on observations obtained with the Georgia State University Center for High Angular Resolution Astronomy Array at Mount Wilson Observatory. The CHARA Array is supported by the National Science Foundation under grant Nos. AST-1636624 and AST-2034336. Institutional support has been provided from the GSU College of Arts and

Sciences and the GSU Office of the Vice President for Research and Economic Development. Time at the CHARA Array was granted through the NOIRLab community access program (NOAO PropIDs: 2017A-0273, 2018A-0286, 2018B-0218, 2020A-0379; NOIRLab PropID: 2021A-0276; PI: E. Sandquist). MIRC-X received funding from the European Research Council (ERC) under the European Union's Horizon 2020 research and innovation program (grant No. 639889). J.D. M. acknowledges funding for the development of MIRC-X (NASA-XRP NNX16AD43G, NSF-ATI 1506540, NSF-AST 1909165). S.K. acknowledges support from an ERC Consolidator Grant (grant agreement No. 101003096). A.L. received support from a Science Technology and Facilities Council (STFC) studentship (No. 630008203). L.R.B. acknowledges support by MIUR under PRIN program No. 2017Z2HSMF.

Facilities: CHARA (CLIMB, MIRC-X), KPNO:CFT, NOT (FIES), OHP (ELODIE).

Software: BF-rvplotter (https://github.com/mrawls/BF-rvplotter), FIESTool.

Appendix
Bright Main-sequence and Subgiant Stars in Praesepe and the Hyades

In order to make the cleanest CMD comparison between the two clusters, we need to understand whether the photometry of the most age-sensitive stars is affected by binarity. Most of the bright stars have been claimed to be close binaries, but in many cases the evidence is rather marginal. We discuss the current evidence below, proceeding from most to least luminous stars.

A.1. Praesepe Members

35 Cnc/HD 72779/VL 133: This star is a fairly rapidly rotating subgiant star in the red half of the Hertzsprung gap. Radial velocity monitoring by Abt & Willmarth (1999) indicates a constant radial velocity, while lunar occultation observations (Eitter & Beavers 1974; Blow et al. 1982) and speckle interferometry (Mason et al. 1993a) have not shown evidence of a companion.

38 Cnc/BT Cnc/HD 73575/KW 204: Abt & Willmarth (1999) report that this star has no velocity variability but does show line profile variations. This may relate to its δ Sct variability. Breger et al. (2012) find light variations with full amplitude of about 0.06 mag. No companion was detected during lunar occultations (Peterson & White 1984; Peterson et al. 1989) or speckle interferometry (Mason et al. 1993a).

HD 73210/KW 50: Abt & Willmarth (1999) derive a double-line spectroscopic orbit with a 12-day period for this star. The detection of both stars implies substantial light blending, so that the CMD position will not be representative of single stars. However, the binary has a fairly extreme mass ratio ($q \approx 0.35$), which means that the CMD position of the brighter star does not reside too far from that of the binary. Lunar occultation (Blow et al. 1982) and speckle interferometry (Mason et al. 1993a) did not reveal a companion.

HD 73712/KW 284: Abt & Willmarth (1999) observe a sharp-lined pair of stars in spectra, superimposed on a third component with broad lines. They derive a spectroscopic orbit with a 48-day period for the sharp-lined pair with a mass ratio fairly close to 1. Needless to say, the CMD position does not adequately represent any of the component stars, and all are likely to be near the main sequence. Speckle interferometry (McAlister et al. 1989; Mason et al. 1993a; Hartkopf et al. 1994, 1997, 2000; Tokovinin 2017) and lunar occultation (Peterson et al. 1989) probably show orbital motion of the third star, approximately 1.6 mag fainter with about 0.″1 angular separation.

EP Cnc/HD 73819/KW 348: Similar to 35 Cnc, Abt & Willmarth (1999) report that this star has no velocity variability but rapid line profile variations. This may also relate to its δ Sct variability. The amplitude of the stars's photometric variations is relatively small (~0.01 mag; Breger et al. 2012), however. No companion was detected during lunar occultations (Peterson & White 1984; Peterson et al. 1989).

42 Cnc/HD 73785/KW 328: Abt & Willmarth (1999) report no velocity variation in their extensive observations, in contradiction to an earlier report by Raboud & Mermilliod (1998) that it was an SB2 based on older observations. No companion was detected during lunar occultations (Peterson & White 1984; Peterson et al. 1989).

HD 73449/KW 150: This star has long been known to rotate at greater than 200 km s^{-1}, and it is considerably redder than other cluster stars at the same brightness. A lunar occultation (Peterson & White 1984) and speckle interferometry (Mason et al. 1993a) did not reveal evidence of a companion star. Raboud & Mermilliod (1998) identified it as an SB1 on the basis of old radial velocity measurements, but Abt & Willmarth (1999) found it to have constant radial velocity. The star has been identified as photometrically variable in the older literature, but recent studies have used it as a constant photometric comparison star for δ Sct studies (Hernandez et al. 1998; Pena et al. 1998).

HD 72942/KW 534: HD 72942 is a known single-lined spectroscopic binary with an orbital period of 131.96 days (Abt & Willmarth 1999), indicating a lack of interaction between the stars. The fact that the binary's color is bluer than any main-sequence star also implies that the primary star must be one of the bluest stars in the cluster. The star has an interesting hybrid surface composition between normal A stars and Am stars (Fossati et al. 2007). In addition, the primary star is rotating at a rate that puts it toward the high end of the range for the cluster's Am stars (Fossati et al. 2008). These items leave a somewhat ambiguous picture of the star's nature, but a blue straggler history cannot be ruled out. A lunar occultation (Peterson & White 1984) and speckle interferometry observations (Mason et al. 1993a) were negative for a companion. We conclude that this star probably should not be considered a representative of single cluster stars.

HD 72846: This star had a composition study by Fossati et al. (2008), who found it to be consistent with normal main-sequence abundances in the cluster. No evidence of binarity for this star has yet been found in speckle interferometry observations (Mason et al. 1993a), and a small number of radial velocity measurements are consistent with a constant value (Abt 1970).

HD 73711/KW 276: This star has abundances consistent with chemically peculiar Am stars (Burkhart & Coupry 1998; Fossati et al. 2007), and as with many of those, there are tentative signs of binarity in spectra. Burkhart & Coupry (1998) identified the star as SB2 based on line profiles, while Raboud & Mermilliod (1998) identified it as SB1 based on variation in older radial velocities. No velocity variations were found in the observations by Abt & Willmarth (1999), although they saw

evidence of asymmetries in the line profiles. Lunar occultation (Peterson & White 1984) and speckle interferometry (Mason et al. 1993a) did not reveal a companion.

A.2. Hyades Members

δCas/37 Cas/HD 8538: This star is apart from the main body of the cluster and was recently identified as a member of the preceding tidal tail of the cluster (Röser et al. 2019). Its position in the Hertzsprung gap makes it interesting for isochrone fitting. The star does not appear to be velocity variable (Abt 1965). Although it is identified as an eclipsing variable in SIMBAD, there is no strong evidence that it is photometrically variable (Samus et al. 2017). To date, the evidence is that it is a single star, although there is no high-resolution imaging or interferometry in the literature.

θ^2 Tau/78 Tau/HD 28319/vB 72: This is a very well-known spectroscopic and interferometrically resolved binary. The most recent analyses of the binary are in Torres et al. (2011) and Armstrong et al. (2006). Although the photometry of the two components can potentially be disentangled, this is beyond the scope of this work.

κ^1 Tau/65 Tau/HD 27934/vB 54: This star is identified as probably velocity constant in Abt (1965). The only reference to binarity is a report from a visual observation of a lunar occultation (Dunham 1974) that reported the minimum resolvable separation ($0\farcs1$) and equal brightness components. Attempts at speckle interferometry detections have been negative (Hartkopf & McAlister 1984; Mason et al. 1993b; Patience et al. 1998). We conclude that there is not significant evidence of binarity for this star.

δ^3 Tau A/68 Tau/HD 27962/vB 56: This star is identified as a cluster blue straggler based on its very blue color, as well as an Am star, and so we do not consider it in discussing the cluster age. It is a velocity variable (Borgniet et al. 2019), but there have only been negative detections of a close companion in lunar occultations (Trunkovsky 2013) and speckle interferometry (Hartkopf & McAlister 1984; Mason et al. 1993b; Patience et al. 1998).

ιTau/102 Tau/HD 32301/vB 129: 102 Tau was shown to have constant radial velocity in Abt (1965). Speckle interferometry observations have not revealed a close companion (Hartkopf & McAlister 1984; Mason et al. 1993b; Patience et al. 1998). There is a report of a lunar occultation in 1956 that indicated two equal-brightness stars at $0\farcs4$ separation (Hoffleit & Jaschek 1991), although this seems to contradict the negative speckle results. At present, the evidence for a companion star with significant brightness is minimal.

c Tau/90 Tau/HD 29388/vB 104: We ignore the wide common proper-motion components in this discussion. A faint companion was detected interferometrically by Marion et al. (2014) at a separation of 11 mas, contributing only about 3% in *H* band. 90 Tau was reported early on as a spectroscopic binary (Barrett 1910) but is labeled as a "constant:" velocity star in Abt (1965). Based on the evidence, we expect the interferometric companion to have little effect on the system photometry in the optical, but it is unclear whether there is a closer companion affecting the velocities.

σ^2 Tau/92 Tau/HD 29488/vB 108: 92 Tau was identified by Lee (1909) as a double-lined spectroscopic binary but later shown by Abt (1965) to have constant velocity. Borgniet et al. (2019) identify low-level velocity variations ($\sim$1 km s^{-1}) from more recent data covering 1370 days, and Lagrange et al. (2009) identify it as velocity variable but not as a binary candidate. Speckle interferometric observations have not detected a companion (Mason et al. 1993b; Patience et al. 1998). We conclude that there may be a companion to the star but that it is likely to be faint based on the lack of spectroscopic detections.

λGem/54 Gem/HD 56537: This is a star identified in the trailing tail of the Hyades (Röser et al. 2019). It was identified early as a spectroscopic binary with a period of 4–5 days by Hnatek (1913), and again by Frost (1924), with other indications of velocity variations in Abt (1970). Lagrange et al. (2009) did not identify it as a binary candidate from more recent radial velocity measurements, nor did Becker et al. (2015). While there is a visual companion at $10''$ separation, a closer companion has been resolved by lunar occultation: initially by Dunham (1977) and then by Richichi et al. (1999) following several negative results. Dunham initially identified the closer companion as visually fainter by 1 mag, but Richichi et al. found it fainter in *K* by about 3.4 mag. Both studies found separations of tens of milliarcseconds. The companion was not detected in other ground-based interferometer measurements (Marion et al. 2014). Based on the evidence, we expect the companion to have a small effect on the system photometry.

θCas/33 Cas/HD 6961: This star is in the preceding tidal tail of the cluster (Röser et al. 2019) and was identified as a long-period single-lined spectroscopic binary by Abt (1965) and Abt & Levy (1974). More recently, Borgniet et al. (2019) found no significant radial velocity variation over a 1417-day baseline. Speckle interferometry studies have not revealed a close companion (Hartkopf & McAlister 1984). The star is used as a calibrator for interferometric studies, and there have been no reports of binarity. We conclude that there may be low-level contamination of the light of the primary star.

HD 30210/vB 112: We will ignore two wide common proper-motion companions in this discussion. This star was identified in the trailing tail of the cluster (Röser et al. 2019). It is also a known Am star, which generally have higher probabilities of binarity than single stars. Abt & Levy (1974) identify it as a single-lined spectroscopic binary with uncertain orbital elements. Speckle observations (Mason et al. 1993b) gave negative results for a companion. Based on the potential color effects of being an Am star and the chance that the spectroscopic companion might affect the photometry, we leave it out of consideration for age purposes.

δ^2 Tau/64 Tau/HD 27819/vB 47: This star was identified as a likely spectroscopic binary by Lee (1909) but was identified as velocity constant in Abt (1965) with a chance of slow variation. Borgniet et al. (2019) find evidence of low-amplitude velocity variations over a 1399-day span, but inconsistent with the earlier Lee measurements. A lunar occultation observation (Africano et al. 1978) and speckle interferometry (Hartkopf & McAlister 1984; Mason et al. 1993b) were negative for a companion. We conclude that there may be low-level effects on the photometry of the primary star.

HD 28527/vB 82: This star is labeled as a δ Sct variable in SIMBAD, but it appears to be a constant star (Kovacs & Paparo 1989). It was identified as a possible binary by Barrett (1910) but later labeled as velocity constant in Abt (1965). Multiple lunar occultation observations (White 1979; Fekel et al. 1980; Radick & Lien 1980; Evans & Edwards 1981; Radick et al. 1982; Richichi et al. 1999) have been negative for a companion, while Peterson et al. (1981) provide "strong, but

not definitive" evidence of a companion with fairly large magnitude difference (∼3 mag) at very small separation. We conclude that the weight of the evidence is against a bright, close companion.

ORCID iDs

Leslie M. Morales https://orcid.org/0000-0002-1333-8866
Eric L. Sandquist https://orcid.org/0000-0003-4070-4881
Gail H. Schaefer https://orcid.org/0000-0001-5415-9189
Christopher D. Farrington https://orcid.org/0000-0001-9939-2830
Robert Klement https://orcid.org/0000-0002-4313-0169
Luigi R. Bedin https://orcid.org/0000-0003-4080-6466
Mattia Libralato https://orcid.org/0000-0001-9673-7397
Luca Malavolta https://orcid.org/0000-0002-6492-2085
Domenico Nardiello https://orcid.org/0000-0003-1149-3659
Jerome A. Orosz https://orcid.org/0000-0001-9647-2886
John D. Monnier https://orcid.org/0000-0002-3380-3307
Stefan Kraus https://orcid.org/0000-0001-6017-8773
Jean-Baptiste Le Bouquin https://orcid.org/0000-0002-0493-4674
Narsireddy Anugu https://orcid.org/0000-0002-2208-6541
Theo ten Brummelaar https://orcid.org/0000-0002-0114-7915
Claire L. Davies https://orcid.org/0000-0001-9764-2357
Jacob Ennis https://orcid.org/0000-0002-1575-4310
Tyler Gardner https://orcid.org/0000-0002-3003-3183
Cyprien Lanthermann https://orcid.org/0000-0001-9745-5834

References

Abt, H. A. 1965, ApJS, 11, 429
Abt, H. A. 1970, ApJS, 19, 387
Abt, H. A. 1986, PASP, 98, 307
Abt, H. A., & Levy, S. G. 1974, ApJ, 188, 291
Abt, H. A., & Willmarth, D. W. 1999, ApJ, 521, 682
Africano, J. L., Evans, D. S., Fekel, F. C., Smith, B. W., & Morgan, C. A. 1978, AJ, 83, 1100
Agüeros, M. A., Covey, K. R., Lemonias, J. J., et al. 2011, ApJ, 740, 110
Anugu, N., Le Bouquin, J.-B., Monnier, J. D., et al. 2020, AJ, 160, 158
Armstrong, J. T., Mozurkewich, D., Hajian, A. R., et al. 2006, AJ, 131, 2643
Avni, Y. 1976, ApJ, 210, 642
Bailer-Jones, C. A. L., Rybizki, J., Fouesneau, M., Demleitner, M., & Andrae, R. 2021, AJ, 161, 147
Barrett, S. B. 1910, ApJ, 32, 183
Becker, J. C., Johnson, J. A., Vanderburg, A., & Morton, T. D. 2015, ApJS, 217, 29
Belmonte, J. A., Michel, E., Alvarez, M., et al. 1994, A&A, 283, 121
Bessell, M. S., Castelli, F., & Plez, B. 1998, A&A, 333, 231
Blow, G. L., Chen, P. C., Edwards, D. A., Evans, D. S., & Frueh, M. 1982, AJ, 87, 1571
Boesgaard, A. M., Roper, B. W., & Lum, M. G. 2013, ApJ, 775, 58
Borgniet, S., Lagrange, A. M., Meunier, N., et al. 2019, A&A, 621, A87
Bourges, L., Mella, G., Lafrasse, S., et al. 2017, VizieR Online Data Catalog: II/346
Brandt, T. D., & Huang, C. X. 2015, ApJ, 807, 24
Breger, M., Hareter, M., Endl, M., et al. 2012, AN, 333, 131
Bressan, A., Marigo, P., Girardi, L., et al. 2012, MNRAS, 427, 127
Brogaard, K., Bruntt, H., Grundahl, F., et al. 2011, A&A, 525, A2
Brogaard, K., VandenBerg, D. A., Bruntt, H., et al. 2012, A&A, 543, A106
Burkhart, C., & Coupry, M. F. 1998, A&A, 338, 1073
Bush, T. C., & Hintz, E. G. 2008, AJ, 136, 1061
Cantat-Gaudin, T., Jordi, C., Vallenari, A., et al. 2018, A&A, 618, A93
Cardelli, J. A., Clayton, G. C., & Mathis, J. S. 1989, ApJ, 345, 245
Carrera, R., & Pancino, E. 2011, A&A, 535, A30
Castelli, F., & Kurucz, R. L. 2003, in Proc. of the 210th Symp. of the IAU, Modelling of Stellar Atmospheres, ed. N. Piskunov, W. W. Weiss, & D. F. Gray (San Francisco, CA: ASP), A20
Charbonneau, P. 1995, ApJS, 101, 309
Choi, J., Dotter, A., Conroy, C., et al. 2016, ApJ, 823, 102
Clampitt, L., & Burstein, D. 1997, AJ, 114, 699
Coelho, P., Bruzual, G., Charlot, S., et al. 2007, MNRAS, 382, 498
Cohen, M., Wheaton, W. A., & Megeath, S. T. 2003, AJ, 126, 1090
Cummings, J. D., Deliyannis, C. P., Maderak, R. M., & Steinhauer, A. 2017, AJ, 153, 128
Cummings, J. D., Kalirai, J. S., Tremblay, P. E., Ramirez-Ruiz, E., & Choi, J. 2018, ApJ, 866, 21
de Boer, K. S., & Wesselius, P. R. 1980, AJ, 85, 1354
de Bruijne, J. H. J., & Eilers, A. C. 2012, A&A, 546, A61
Debernardi, Y., Mermilliod, J. C., Carquillat, J. M., & Ginestet, N. 2000, A&A, 354, 881
Delorme, P., Collier Cameron, A., Hebb, L., et al. 2011, MNRAS, 413, 2218
D'Orazi, V., Oliva, E., Bragaglia, A., et al. 2020, A&A, 633, A38
Douglas, S. T., Agüeros, M. A., Covey, K. R., & Kraus, A. 2017, ApJ, 842, 83
Douglas, S. T., Curtis, J. L., Agüeros, M. A., et al. 2019, ApJ, 879, 100
Dunham, D. W. 1974, OccN, 1, 4
Dunham, D. W. 1977, OccN, 1, 119
Eitter, J. J., & Beavers, W. I. 1974, ApJS, 28, 405
Evans, D. S., & Edwards, D. A. 1981, AJ, 86, 1277
Evans, D. S., & Edwards, D. A. 1983, AJ, 88, 1845
Evans, D. S., Edwards, D. A., Frueh, M., McWilliam, A., & Sandmann, W. H. 1985, AJ, 90, 2360
Fekel, F. C., Montemayor, T. J., Barnes, T. G. I., & Moffett, T. J. 1980, AJ, 85, 490
Finkbeiner, D. P., Schlafly, E. F., Schlegel, D. J., et al. 2016, ApJ, 822, 66
Fossati, L., Bagnulo, S., Landstreet, J., et al. 2008, A&A, 483, 891
Fossati, L., Bagnulo, S., Monier, R., et al. 2007, A&A, 476, 911
Frandsen, S., Pigulski, A., Nuspl, J., et al. 2001, A&A, 376, 175
Frost, E. B. 1924, ApJ, 60, 319
Gaia Collaboration, Babusiaux, C., van Leeuwen, F., et al. 2018, A&A, 616, A10
Gáspár, A., Rieke, G. H., Su, K. Y. L., et al. 2009, ApJ, 697, 1578
Gossage, S., Conroy, C., Dotter, A., et al. 2018, ApJ, 863, 67
Gray, R. O. 1998, AJ, 116, 482
Grenier, S., Baylac, M. O., Rolland, L., et al. 1999, A&AS, 137, 451
Hartkopf, W. I., Mason, B. D., McAlister, H. A., et al. 2000, AJ, 119, 3084
Hartkopf, W. I., & McAlister, H. A. 1984, PASP, 96, 105
Hartkopf, W. I., McAlister, H. A., Mason, B. D., et al. 1994, AJ, 108, 2299
Hartkopf, W. I., McAlister, H. A., Mason, B. D., et al. 1997, AJ, 114, 1639
Henden, A. A. 2019, JAVSO, 47, 130
Hernandez, M. M., Michel, E., Belmonte, J. A., et al. 1998, A&A, 337, 198
Hidalgo, S. L., Pietrinferni, A., Cassisi, S., et al. 2018, ApJ, 856, 125
Hnatek, A. 1913, AN, 195, 171
Hoffleit, D., & Jaschek, C. 1991, The Bright Star Catalogue (5th Edition; New Haven, CT: Yale Univ. Observatory)
Hog, E., Kuzmin, A., Bastian, U., et al. 1998, A&A, 335, L65
Horch, E. P., Casetti-Dinescu, D. I., Camarata, M. A., et al. 2017, AJ, 153, 212
Hui-Bon-Hoa, A., & Alecian, G. 1998, A&A, 332, 224
Ishihara, D., Onaka, T., Kataza, H., et al. 2010, A&A, 514, A1
Johnson, H. L., & Mitchell, R. I. 1975, RMxAA, 1, 299
Kazlauskas, A., Straižys, V., Bartašiūtė, S., et al. 2006, BaltA, 15, 511
Klein Wassink, W. J. 1927, PGro, 41, 1
Kluska, J., Kraus, S., Davies, C. L., et al. 2018, ApJ, 855, 44
Kornilov, V. G., Volkov, I. M., Zakharov, A. I., et al. 1991, TrSht, 63, 1
Kovács, G., Hartman, J. D., Bakos, G. Á, et al. 2014, MNRAS, 442, 2081
Kovacs, G., & Paparo, M. 1989, MNRAS, 237, 201
Kraft, R. P. 1967, ApJ, 150, 551
Kraus, S., Monnier, J. D., Anugu, N., et al. 2018, Proc. SPIE, 10701, 1070123
Lagrange, A. M., Desort, M., Galland, F., Udry, S., & Mayor, M. 2009, A&A, 495, 335
Lee, O. J. 1909, ApJ, 29, 240
Lindegren, L., Bastian, U., Biermann, M., et al. 2021, A&A, 649, A4
Lindegren, L., Hernández, J., Bombrun, A., et al. 2018, A&A, 616, A2
Mann, A. W., & von Braun, K. 2015, PASP, 127, 102
Marion, L., Absil, O., Ertel, S., et al. 2014, A&A, 570, A127
Martin, D. C., Fanson, J., Schiminovich, D., et al. 2005, ApJL, 619, L1
Mason, B. D., Hartkopf, W. I., McAlister, H. A., & Sowell, J. R. 1993a, AJ, 106, 637
Mason, B. D., McAlister, H. A., Hartkopf, W. I., & Bagnuolo, W. G. J. 1993b, AJ, 105, 220
Mason, B. D., Wycoff, G. L., Hartkopf, W. I., Douglass, G. G., & Worley, C. E. 2001, AJ, 122, 3466

McAlister, H. A., Hartkopf, W. I., Sowell, J. R., Dombrowski, E. G., & Franz, O. G. 1989, AJ, 97, 510
McGee, J. D., Khogali, A., Baum, W. A., & Kraft, R. P. 1967, MNRAS, 137, 303
Monnier, J. D., Che, X., Zhao, M., et al. 2012, ApJL, 761, L3
Monnier, J. D., Zhao, M., Pedretti, E., et al. 2011, ApJL, 742, L1
Morel, M., & Magnenat, P. 1978, A&AS, 34, 477
Morrissey, P., Conrow, T., Barlow, T. A., et al. 2007, ApJS, 173, 682
Oke, J. B., & Gunn, J. E. 1983, ApJ, 266, 713
Orosz, J. A., & Hauschildt, P. H. 2000, A&A, 364, 265
Patience, J., Ghez, A. M., Reid, I. N., Weinberger, A. J., & Matthews, K. 1998, AJ, 115, 1972
Paunzen, E. 2015, A&A, 580, A23
Pena, J. H., Peniche, R., Hobart, M. A., et al. 1998, A&AS, 129, 9
Peterson, D. M., Baron, R., Dunham, E. W., et al. 1989, AJ, 98, 2156
Peterson, D. M., Baron, R. L., Dunham, E., et al. 1981, AJ, 86, 280
Peterson, D. M., & White, N. M. 1984, AJ, 89, 824
Plaskett, J. S., Harper, W. E., Young, R. K., & Plaskett, H. H. 1921, PDAO, 1, 287
Raboud, D., & Mermilliod, J. C. 1998, A&A, 333, 897
Rachford, B. L. 1998, ApJ, 505, 255
Radick, R., & Lien, D. 1980, AJ, 85, 1053
Radick, R. R., Africano, J. L., Rogers, W. F., Schneeberger, T. J., & Tyson, E. T. 1982, AJ, 87, 885
Rawls, M. 2016, BF-rvplotter, GitHub, https://github.com/mrawls/BF-rvplotter
Richichi, A., Ragland, S., Calamai, G., et al. 1999, A&A, 350, 491
Rodrigo, C., & Solano, E. 2020, in Contributions to the XIV.0 Scientific Meeting (Virtual) of the Spanish Astronomical Society (Barcelona: Spanish Astronomical Society), 182
Rodrigo, C., Solano, E., & Bayo, A. 2012, SVO Filter Profile Service Version 1.0, doi: 10.5479/ADS/bib/2012ivoa.rept.1015R
Röser, S., & Schilbach, E. 2019, A&A, 627, A4
Röser, S., Schilbach, E., & Goldman, B. 2019, A&A, 621, L2
Royer, F., Grenier, S., Baylac, M. O., Gómez, A. E., & Zorec, J. 2002, A&A, 393, 897
Rucinski, S. M. 1992, AJ, 104, 1968
Rufener, F. 1988, Catalogue of Stars Measured in the Geneva Observatory Photometric System (Sauverny: Observatoire de Geneve), 4
Salaris, M., & Bedin, L. R. 2019, MNRAS, 483, 3098
Samus, N. N., Kazarovets, E. V., Durlevich, O. V., Kireeva, N. N., & Pastukhova, E. N. 2017, ARep, 61, 80
Schaefer, G. H., Hummel, C. A., Gies, D. R., et al. 2016, AJ, 152, 213
Scholz, A., & Eislöffel, J. 2007, MNRAS, 381, 1638
Scholz, A., Irwin, J., Bouvier, J., et al. 2011, MNRAS, 413, 2595
Skrutskie, M. F., Cutri, R. M., Stiening, R., et al. 2006, AJ, 131, 1163
Taylor, B. J. 2006, AJ, 132, 2453
Telting, J. H., Avila, G., Buchhave, L., et al. 2014, AN, 335, 41
ten Brummelaar, T. A., McAlister, H. A., Ridgway, S. T., et al. 2005, ApJ, 628, 453
Ten Brummelaar, T. A., Sturmann, J., Ridgway, S. T., et al. 2013, JAI, 2, 1340004
Tokovinin, A. 2017, AJ, 154, 110
Torres, K. B. V., Lampens, P., Frémat, Y., et al. 2011, A&A, 525, A50
Trunkovsky, E. M. 2013, ARep, 57, 692
Vejar, G., Schuler, S. C., & Stassun, K. G. 2021, ApJ, 919, 100
Wesselius, P. R., van Duinen, R. J., de Jonge, A. R. W., et al. 1982, A&AS, 49, 427
White, N. M. 1979, AJ, 84, 872
Wright, E. L., Eisenhardt, P. R. M., Mainzer, A. K., et al. 2010, AJ, 140, 1868
Yang, X. L., Chen, Y. Q., & Zhao, G. 2015, AJ, 150, 158
York, D. G., Adelman, J., Anderson, J. E. J., et al. 2000, AJ, 120, 1579
Zinn, J. C., Pinsonneault, M. H., Huber, D., & Stello, D. 2019, ApJ, 878, 136